

Nonlinearity of the post-spinel transition and its expression in slabs and plumes worldwide

Junjie Dong^{1,2,*}, Rebecca A. Fischer¹, Lars Stixrude³, Matthew C. Brennan¹, Kierstin Daviau^{1,a,b}, Terry-Ann Suer^{1,c}, Katlyn M. Turner^{1,d}, Yue Meng⁴, Vitali B. Prakapenka⁵.

¹ Department of Earth and Planetary Sciences, Harvard University, Cambridge, Massachusetts, United States of America.

² Department of the History of Science, Harvard University, Cambridge, Massachusetts, United States of America.

³ Department of Earth, Planetary, and Space Sciences, University of California, Los Angeles, California, United States of America.

⁴ High Pressure Collaborative Access Team (HPCAT), X-Ray Science Division, Argonne National Laboratory, Argonne, Illinois, United States of America.

⁵ Center for Advanced Radiation Sources, University of Chicago, Chicago, Illinois, United States of America.

^a Now at Toi-Ohomai Institute of Technology, Tauranga, New Zealand.

^b Now at School of Science, University of Waikato, Tauranga, New Zealand.

^c Now at Laboratory for Laser Energetics, University of Rochester, Rochester, New York, United States of America.

^d Now at MIT Media Lab, Massachusetts Institute of Technology, Cambridge, Massachusetts, United States of America.

* Corresponding author: Junjie Dong (junjiedong@g.harvard.edu)

Keywords: post-spinel transition; 660-km discontinuity; Clapeyron slope; phase diagram; machine learning; logistic regression

Abstract

At the interface of Earth's upper and lower mantle, the post-spinel transition boundary controls the dynamics and morphologies of downwelling slabs and upwelling plumes, and its Clapeyron slope is hence one of the most important constraints on mantle convection. In this study, we reported a new in situ experimental dataset on phase stability in Mg_2SiO_4 at mantle transition zone pressures from laser-heated diamond anvil cell experiments, along with a compilation of corrected in situ experimental datasets from the literature. We presented a machine learning framework for high-pressure phase diagram determination and focused on its application to constrain the location and Clapeyron slope of the post-spinel transition: ringwoodite \leftrightarrow bridgmanite + periclase. We found that the post-spinel boundary is nonlinear and its Clapeyron slope varies locally from $-2.3_{-1.4}^{+0.6}$ MPa/K at 1900 K, to $-1.0_{-1.7}^{+1.3}$ MPa/K at 1700 K, and to $0.0_{-2.0}^{+1.7}$ MPa/K at 1500 K. We applied the temperature-dependent post-spinel Clapeyron slope to

estimate its lateral variation across the “660-km” seismic discontinuity in subducting slabs and hotspot-associated plumes worldwide, as well as the ambient mantle. We found that, in the present-day mantle, the average post spinel Clapeyron slope in the plumes is three times more negative than that in slabs, and we then discussed the effects of a nonlinear post-spinel transition on the dynamics of Earth’s mantle.

1 Introduction

The pressure-induced, endothermic breakdown of ringwoodite (rw) into bridgmanite and ferropericlase ($bm + fp$) in the iron-bearing system $(Mg,Fe)_2SiO_4$, typically referred to as the post-spinel transition, coincides with a global scale seismic discontinuity in the Earth’s mantle at approximately 660 km in depth (e.g., Deuss et al., 2013). Significant changes in temperature, rheology, and buoyancy accompany the post-spinel transition and influence mantle circulation through interaction with cold downwelling (slabs) and hot upwelling (plumes). The reaction pressure of the post-spinel transition in $(Mg,Fe)_2SiO_4$ is nearly independent of the presence of iron in small amounts (e.g., <0.01 GPa at 1700 K, corresponding to <250 m in the mantle, Ishii et al., 2019). Hence, the pressure (P) and temperature (T) conditions and Clapeyron slope of the $rw \leftrightarrow bm + \text{periclase } (pe)$ boundary in the iron-free system Mg_2SiO_4 , can be used as a proxy to investigate the interactions of the mantle transition zone with slabs and plumes.

Several generations of experimentalists have studied the location and Clapeyron slope of the $rw \leftrightarrow bm + pe$ post-spinel transition, along with other solid-solid phase transitions/reactions in Mg_2SiO_4 at transition zone pressures: wadsleyite (wd) $\leftrightarrow rw$ and $wd \leftrightarrow bm + pe$, using ex situ (quench) or in situ experiments in multi-anvil (MA) press (Ito & Takahashi, 1989; Irifune et al., 1998; Suzuki et al., 2000; Hirose, 2002; Katsura et al., 2003; Fei et al., 2004; Inoue et al., 2006; Ishii et al., 2011; Ghosh et al., 2013) as well as in situ experiments in laser-heated diamond anvil cell (DAC) (Shim et al., 2001; Chudinovskikh & Boehler, 2001). Despite several decades of experimental focus on one phase diagram, there is not yet a global analysis of phase stability observations in Mg_2SiO_4 that provides a statistically-optimized Mg_2SiO_4 phase diagram and determines its phase boundaries and their uncertainties self-consistently. Furthermore, the post-spinel boundary has historically been conceived as a linear boundary, but a recent experimental dataset reported by Chanyshv et al., (2022) suggests that the post-spinel boundary is *not* linear based on free-hand drawing. A robust assessment of the nonlinearity of the post-spinel boundary therefore becomes indispensable for more realistic morphological and dynamical interpretation of slabs and plumes.

In this paper, we first reported a new set of the Mg_2SiO_4 phase diagram data (Section 2). This dataset covers the P – T range (16–28 GPa, 1573–2723 K) for all three phase transitions at transition zone pressures and includes the high temperature area between the triple point and the Mg_2SiO_4 solidus ($>\sim 2000$ K) that has not been well constrained by previous studies. Then, we proposed a machine learning framework for high-pressure phase diagram determination. In combination with previously published experimental datasets (Section 3), we applied this novel analytical methodology to determine the locations and Clapeyron slopes of these phase

transitions in Mg_2SiO_4 and the corresponding triple point (Section 4). Most importantly, we obtained a robust estimate on the nonlinearity of the post-spinel transition Clapeyron slope and its associated uncertainty, and then estimated the lateral variation of the post-spinel Clapeyron slope in subducting slabs, hotspot-associated plumes, as well as the ambient mantle at the base of the transition zone (Section 5).

2 New in situ experimental dataset on the Mg_2SiO_4 phase diagram

2.1 Synchrotron X-ray diffraction experiments

Our experimental dataset on the Mg_2SiO_4 phase diagram was collected in laser-heated DAC experiments (LH-DAC) with in situ X-ray diffraction (XRD) at high pressure and high temperature. Short symmetric cells and a gas-membrane cell were used to generate high pressure. Double-sided laser heating and synchrotron XRD measurements were performed at beamline 13-ID-D of GeoSoilEnviro Center for Advanced Radiation Sources (GSECARS) (Shen et al., 2005; Prakapenka et al., 2008), and beamline 16-ID-B, High Pressure Collaborative Access Team (HPCAT) (Meng et al., 2015) at the Advanced Photon Source (APS), Argonne National Laboratory (ANL). Starting materials were powdered synthetic forsterite Mg_2SiO_4 mixed with tungsten (W). The mixed sample was sandwiched between two potassium chloride (KCl) layers and loaded in a sample chamber pre-dilled in a rhenium (Re) gasket. The KCl layers served as the pressure medium, thermal insulator, and the primary pressure scale while the W powder was used as a laser absorber and a secondary pressure scale. Both W and KCl have melting temperatures higher than those of Mg_2SiO_4 (Errandonea et al., 2002; Zhou et al., 2020) and are chemically inert at the relevant pressure and temperature range. More details of our experimental setup can be found in Supplementary Text S1.

Sample temperatures (T_{meas}) were measured spectroradiometrically, and temperatures of the KCl layers (T_{KCl}) were estimated¹ from the mean temperatures between the sample (T_{meas}) and the diamond anvil culets, whose surface temperatures are 295 K (Campbell et al., 2009). Sample pressures P_{W} and P_{KCl} were determined based on the equation of state (EoS) of W with T_{meas} (Sokolova et al., 2016) and the EoS of KCl with T_{KCl} (Tateno et al., 2019, cross-calibrated with Sokolova et al., 2016), respectively. The estimated P_{W} deviates from P_{KCl} significantly at high temperatures (Fig. S1), likely due to lack of thermal EoS data on W at $>\sim 1673$ K (Litasov et al., 2013; Sokolova et al., 2016). Therefore, we chose KCl as our primary pressure scale, and all pressures reported in the main text are based on the EoS of KCl from Tateno et al., (2019). The unit cell parameters of both KCl and W and their estimated pressures can be found in Table S1.

2.2 Phase boundary detection

¹ The equation to estimate the effective temperature through the salt pressure medium proposed by Campbell et al. (2009) contains a typo, and the correct formula to calculate T_{KCl} should be written as follows:

$$T_{\text{KCl}} = \frac{3T_{\text{meas}} + 295}{4} \pm \frac{T_{\text{meas}} - 295}{4}.$$

Here, we reported a new dataset of phase stability observations for Mg_2SiO_4 between 16 and 28 GPa and between 1573 and 2723 K (Fig. 1). These in situ phase stability observations were collected upon heating and/or compression from 9 LH-DAC experiments with 17 laser-heated spots. The P - T path of each experiment is shown in Fig. 1*c-i*, and further details (including unit cell parameters and uncertainties) are available in Table S1. In a typical experiment with the short symmetric cell (Fig. 1, *d, f, g, h, j*, and *k*), we first compressed the sample to a target pressure (usually 16–22 GPa) and then pre-heated the sample to 1200–1500 K until the diffraction peaks of either wd or rw became clear. After that, we began the heating cycle by increasing temperature slowly while continuously taking diffraction patterns. Three of our experiments, D1m, D4m, and D11m, were conducted in a gas-membrane cell; they were first heated up to 2000–2200 K at some pressures lower than 20–21 GPa, and then very small incremental loads were applied from a gas membrane system to increase the pressure remotely while the sample was being heated (Fig. 1, *c, e* and *i*).

In Figure 1, we showed two examples of our in situ phase stability observations in which phase transitions were detected between two consecutive diffraction patterns upon heating. Figure 1a shows the $wd \leftrightarrow rw$ transition: all visible diffraction peaks of D13_S2_005 can be attributed to wd , and wd is the only stable phase at 1616 K, 20.6 GPa. In the next diffraction pattern, D13_S2_006, the rw peaks appeared in the heating cycle for the first time, and wd began transforming into rw at 1785 K, 21.0 GPa. Figure 1b shows the $rw \leftrightarrow bm + pe$ post-spinel transition near the triple point. Here, the rw peaks of D13_S2_010 at 2052 K, 21.9 GPa continued to grow from D13_S2_006 at 1785 K, 21.0 GPa but became increasingly overlapped with the wd peaks at high temperatures (e.g., wd (040) and rw (220)). In the next diffraction pattern, D13_S2_011, the bm peaks appeared in the heating cycle for the first time, and rw began transforming into bm (+ pe) at 2173 K, 22.2 GPa. The relics of the wd phase remained in the diffraction pattern, and a few peaks grew significantly (123) or reappeared (211) upon heating. The pe peaks were rarely found in the diffraction patterns at the first appearance of the bm peaks due to their overlap with silicate peaks. Additional details of phase identification and phase boundary detection can be found in Supplementary Text S2.

3 In situ phase stability observations in Mg_2SiO_4 compiled from literature and their pressure and temperature corrections

To compare our experimental observations (Section 2) with literature datasets, we searched and compiled all available in situ experimental data on the phase stability of wd , rw , and $bm + pe$ available (Table S2), corrected the temperatures and pressures originally reported in each study (Table S3), and performed a comprehensive analysis of their inter-run and inter-lab uncertainties (Section 4). These previous in situ high-pressure experiments on Mg_2SiO_4 were conducted with either MA or DAC. Additional details of our data compilation can be found in Supplementary Text S4.

One source of discrepancy among the literature datasets is the use of different pressure scales (MgO, Au, Pt, etc.). Pressure estimates have often been incompatible with each other due

to the lack of cross-calibrated equations of state (EoS) for those pressure scales used (e.g., Fei et al., 2007). Fortunately, most recent studies either reported the unit cell parameters of the pressure scales directly or provided the estimated pressure and the EoS references on which their pressure estimates were based. Therefore, we can recalculate the pressures based on some internally consistent pressure scales (Sokolova et al., 2016; Tateno et al., 2019).

Another source of discrepancy is the use of different temperature-measuring techniques: temperature is determined with a spectroradiometer in DAC experiments and with thermocouples in MA. Thermocouples provide higher precision temperature measurements (smaller random errors) than the spectroradiometer in the DAC experiment, but the pressure effects on the temperature–electromotive force (emf) relationship in commonly-used thermocouples had not been systematically investigated until very recently (Nishihara et al., 2020a; Nishihara et al., 2020b). We used the two abovementioned studies published by Nishihara and others to correct the nominal temperatures originally reported by the type D ($W_{97}Re_3$ – $W_{75}Re_{25}$) and type S ($Pt_{90}Rh_{10}$ –Pt) thermocouples from MA experiments. These models for thermocouple pressure effects were obtained at relatively low temperatures ($<1173K$), the temperature corrections we made here, therefore, are provisional (Table S3).

4 Global analysis of phase stability observations in Mg_2SiO_4

4.1 Multi-class logistic model for high pressure phase diagram determination

In principle, to precisely determine the location of a phase boundary from experiments, a pair of phase stability observations, one on each side of the boundary, would be required. However, such experimental brackets become increasingly difficult to obtain at higher pressures, and the results reported from different runs and different laboratories may not be fully consistent with each other. Thus far, most experimental studies determined the phase boundary based on free-hand drawing across their own experimental brackets, without quantitatively considering the inter-run and inter-lab uncertainties among the literature datasets. This common approach does not get a maximum of information from all the experimental constraints available for phase diagram determination, despite the fact that these high pressure experiments are often expensive and time-consuming; it also does not allow for a comprehensive assessment of the reliability and accuracy of the experimental datasets. Here, we proposed a machine learning framework for the global analysis of phase stability observations with multiple (more than two) stable phases or phase assemblage fields. This analytical methodology consists of multi-class logistic regression (this section) and supervised learning (Section 4.2). We performed a global analysis of the Mg_2SiO_4 phase diagram data, compiled from Section 2 and 3, as a case study to demonstrate our proposed analytical methodology for evaluating and selecting models for a phase diagram as well as estimating the uncertainties associated with each phase boundary.

To build a statistical model to describe the stability fields of a high-pressure phase diagram, the response variable (stable phase) must be categorical instead of numerical, and hence determining the location of a phase boundary should be considered a “classification problem”

(e.g., Bishop, 2006; James et al., 2013) since it involves assigning the observations to one stable mineral phase (discrete and categorical response) at a specific P - T condition (numerical predictor). Kavner & Jeanloz, (1998) and Kavner et al., (2011) pioneered a similar but much simpler analysis of phase stability observations through binary logistic regression and tested it on the melting curve of platinum (Pt). However, their implementation 1) is limited to two stable phases with one phase boundary, 2) requires additional assumptions on the shape of the phase boundary, and 3) does not include necessary procedures to prevent overfitting. For the Mg_2SiO_4 phase diagram, with three stable phases or stability fields, wd , rw , and $bm + pe$ at transition zone conditions, we need to generalize the simple binary logistic model and estimate the probabilities of observing multiple stable phases, $\hat{p}(Y|P,T)$ simultaneously ($Y = k$, where k can be wd , rw , or $bm + pe$) at a given P - T condition. In the multi-class logistic model we propose here, the scenarios that Y belongs (or does not belong) to one specific phase stability field, k , can be modeled as:

$$\hat{p}(Y|P,T) = \begin{cases} 0, & \text{if } Y = k \\ 1, & \text{if } Y \neq k \end{cases} \quad (1)$$

To describe the probability that gives outputs between 0 and 1, we can write the probability of observing phase $Y = k$, $\hat{p}(Y = k|P,T)$ at a given P - T condition as a *logistic* function, $\frac{e^{f(X)}}{1+e^{f(X)}}$, where $f(X)$ is a n^{th} degree polynomial function with two variables, $f(P,T)$:

$$\hat{p}(Y = k|P,T) = \frac{e^{\sum_{i,j=0}^n \beta_{i,j}^k P^i T^j}}{1 + e^{\sum_{i,j=0}^n \beta_{i,j}^k P^i T^j}} \quad (2)$$

Alternatively, Equation (2) can be rewritten as:

$$\ln \frac{\hat{p}(Y = k|P,T)}{1 - \hat{p}(Y = k|P,T)} = \ln \frac{\hat{p}(Y = k|P,T)}{\hat{p}(Y \neq k|P,T)} = \sum_{i,j=0}^n \beta_{i,j}^k P^i T^j = f(P,T) \quad (3)$$

The quantities $\ln \frac{\hat{p}(Y = k|P,T)}{\hat{p}(Y \neq k|P,T)}$ and $\ln \frac{\hat{p}(Y = k|P,T)}{1 - \hat{p}(Y = k|P,T)}$ are called log-odds and logit, respectively.

We can interpret the logistic model as fitting the log-odds or logit as a polynomial function of P and T , $f(P,T)$.

We can then convert probability estimates from three separate models (when $k = wd, rw$ or $bm + pe$, $K=3$) to one set of probability estimates using a multi-class generalization of the logistic function, which is also known as the normalized exponential or the *softmax* function:

$$\hat{p}(Y = k|P,T) = \frac{e^{\sum_{i,j=0}^n \beta_{i,j}^k P^i T^j}}{\sum_{h=1}^K e^{\sum_{i,j=0}^n \beta_{i,j}^h P^i T^j}} \quad (4)$$

The rescaled probability estimates add up to 1. We attribute the stable phase as the class with the largest probability, and the tripe point is recovered at which $\hat{p}(Y = wd) = \hat{p}(Y = rw) = \hat{p}(Y = bm+pe) = \frac{1}{3}$.

The coefficients, β_{ij}^k , are estimated by minimizing a combined negative log-likelihood function, or total cross entropy, $-L$ (Bishop, 2006):

$$-L = -\frac{1}{M} \sum_{m=1}^M \sum_{k=1}^K \{t_{m,k}(y_m = k) \cdot \ln[p_m(y_m = k)] + t_{m,l}(y_i \neq k) \cdot \ln[1 - p_m(y_m \neq k)]\} \quad (5)$$

where $t_{m,l}(y_i = k)$ is 1 if and only if the observation m belongs to phase k , $p_m(y_m = k)$ is the output probability that the observation belongs to phase k , and vice versa; M is the total number of observations. Unlike the binary case (e.g., Kanver, 2010), the multi-class logistic model does not produce a simple, easy-to-interpret analytic solution, therefore the phase boundaries between the three phases and their triple point in Mg_2SiO_4 are determined numerically with a Python package, *scikit-learn* (Pedregosa et al., 2011). A comprehensive review of the multi-class logistic model can be found in James et al. (2013).

4.2 Toward a nonlinear post-spinel transition in Mg_2SiO_4

4.2.1 Thermodynamics of the Clapeyron slope for the post-spinel transition

The Clapeyron slope of a coexistence curve, either a phase transition or a reaction, is uniquely determined by the entropy change (ΔS) of the phase transition/reaction divided by its volume change (ΔV); when P and T are constant and the change in the Gibbs free energy, $\Delta G_{P, T = \text{const.}} = 0$, we have $T\Delta S = \Delta H$, and then γ can be written as:

$$\gamma = \frac{\partial P}{\partial T} = \frac{\Delta S}{\Delta V} = \frac{\Delta H}{T\Delta V} \quad (6)$$

Previous studies (e.g., Ito & Takahashi, 1989; Irifune et al., 1998; Shim et al., 2001; Katsura et al., 2003; Fei et al., 2004; Ishii et al., 2011; Ghosh et al., 2013) often adopted a linear approximation for the post-spinel transition in Mg_2SiO_4 , with visual inspection and free-hand drawing. This assumption of a linear boundary was a reasonable choice, given the considerable inter-run and inter-lab uncertainties in existing experimental datasets and the lack of a robust statistical analysis; this linear assumption has often been justified by the semi-empirical interpretation that the changes in $\Delta S_{\text{post-spinel}}$ and $\Delta V_{\text{post-spinel}}$ along the reaction boundary between rw and $bm + pe$ are small, gradual, and comparable.

However, if we take a closer look at recent empirical thermodynamic models of Mg_2SiO_4 that examined and extrapolated the low-temperature thermodynamic data carefully (e.g., Fabrichnaya, 2008; Kojitani et al., 2016; Kojitani et al., 2017), some of their calculated transitions in Mg_2SiO_4 , the post-spinel transition in particular, have a small but non-negligible

nonlinearity. A recent first-principles calculation suggested an increasingly negative post-spinel Clapeyron slope in Mg_2SiO_4 with higher temperatures (Hernández et al., 2015). This predicted nonlinearity of the post-spinel transition implies that the thermal expansion coefficient (α_{rw}) of rw increases slower than that of bm (α_{bm}) and the volume difference between rw and $bm + pe$ ($\Delta V_{\text{post-spinel}}$) would hence decrease with temperature (Hernández et al., 2015; Belmonte et al., 2022); assuming $\Delta S_{\text{post-spinel}}$ remains approximately constant, $\gamma_{\text{post-spinel}}$ is expected to become more negative with increasing temperature. Such nonlinearity may be small enough to be ignored if we are only interested in an averaged value for the Clapeyron slope within 100–200 K, and evidently, earlier studies indeed focused on bracketing the transition near 1700–1900 K, a temperature range only pertinent to warm slabs and the average temperature in ambient mantle across the “660-km” discontinuity. However, we need to take into account the nonlinearity of the post-spinel transition when we consider it across a range of several hundreds of kelvins because $\Delta V_{\text{post-spinel}}$ may change substantially over the entire mantle temperature range, from cold slabs to the ambient mantle and then to hot plumes. Chanyshv et al. (2022) have revisited the post-spinel transition recently with the state-of-the-art MA technique and reported the first experimental evidence of a nonlinear post-spinel transition. Its estimated nonlinearity, however, is based on the experimentalists’ visual inspection and free-hand drawing only, the robustness of their reported Clapeyron slope and its compatibility with other experimental data needs to be assessed.

4.2.2 A machine learning framework for the nonlinearity of phase boundary

In the multi-class logistic model we proposed for phase diagram determination in Section 4.1, a nonlinear phase boundary can be implemented in the log-odd/logit function (Equation 3), and it is mathematically simplified as a polynomial function of P and T . Ideally, a phase boundary should be described by a function of thermoelastic properties such as thermal expansion coefficient, entropy, heat capacity, etc., which can then be converted into a function of pressure, temperature, and chemical composition. However, it would be cumbersome to obtain analytic approximation of these thermodynamic functions because such conversion would require solving a number of inexplicit functions in the EoS for each phase. For simplicity, we used polynomials (Equation 3) to capture the nonlinearity of the phase boundary without the mathematical burdens to extract a complex analytic solution from physical thermodynamics directly.

Overfitting is often the primary argument against using a polynomial in regression models. The high degree of freedom we introduce to a conventional analysis would allow the model to capture not only the location of the phase boundary, but also the noise in the experimental dataset. As the degree of the polynomial keeps increasing, we would begin to fit a squiggle that matches more data points, despite the fact that only a smooth curve is expected for a phase boundary thermodynamically. On the contrary, this proposed machine learning framework is a robust way to identify the shape of a phase transition and to estimate its magnitude. Here, we applied a set of supervised learning algorithms from common machine

learning practices to avoid overfitting, accompanied with regularization and bootstrapping: 1) we first split the compiled dataset into a train set and a test set (70% and 30%). The train set is further divided into k -fold ($k = 3-5$) for cross validation as well as (hyper-)parameter tuning to produce an optimized model for a series of polynomial functions with different degrees ($n = 1-5$), while the test set remained unseen to the models. Then, we used the test set to make the final selection of the best degree of polynomials based on the classification scores of the test set, F_1 score, a harmonic mean of *precision* and *recall*, where an F_1 score reaches its best value at 1 and worst score at 0. To further limit the behavior of the high-order polynomials, we applied L_1 regularization method (*lasso*) to allow the coefficients of some high-order terms to shrink to zero (truncation of high-order terms) when necessary. Finally, we used the selected model with the best degree of polynomials (regularized) to fit the entire dataset (Fig. 2).

During model selection, we used grid search to exhaustively consider all parameter and hyperparameter combinations for the multi-class logistic model, including the degree of polynomials (n), regularization strength (C), and optimization solvers. The regularized 3rd order polynomial (with $C = 1000$ and some high-order terms truncated by L_1 regularization) is found to be the best model to describe the Mg_2SiO_4 phase diagram, with the highest F_1 scores of 0.78 for the test set and 0.82 for the train set. In Fig. 3, the linear and 2nd order polynomial phase boundaries (polynomial with degrees 1 and 2) are insufficient to fit the training data (underfitting). For higher degrees, the models become stabilized but overfit the training data (with high F_1 scores for the training data and lower F_1 scores for the unseen testing data). Definitions and additional details of parameter tuning, regularization, and model selection can be found in Supplementary Text S4. A schematic diagram of the model selection procedures is shown in Fig. S2; nevertheless, a full description of supervised learning algorithms cannot be done here as comprehensively as in textbooks, for example, James et al., (2013).

With the selected best model, we estimated the uncertainty in our predicted phase boundaries using bootstrapping. We resampled the compiled dataset with replacement (67%) and created 5×10^3 copies of the bootstrapped dataset. We then fit the best model to each resampled copy of the dataset, resulting in 5×10^3 sets of phase boundaries. We reported 10–90% confidence intervals of the simulated distributions as the allowed P – T regions (or uncertainty) for the phase boundaries.

4.3 Machine learned phase diagram of Mg_2SiO_4 at transition zone conditions

From the machine-learned phase diagram of Mg_2SiO_4 (Figure 2), we found that the Clapeyron slope of the $rw \leftrightarrow bm + pe$ post-spinel transition varies locally from $-2.3^{+0.6}_{-1.4}$ MPa/K at 1900 ± 50 K, to $-1.0^{+1.3}_{-1.7}$ MPa/K at 1700 ± 50 K, and to $0.0^{+1.7}_{-2.0}$ MPa/K at 1500 ± 50 K, and that the $wd \leftrightarrow rw$ boundary and the $wd \leftrightarrow bm + pe$ boundary are approximately linear, with estimated slopes of $6.2^{+1.6}_{-1.1}$ MPa/K at 1800 ± 200 K and $0.4^{+1.8}_{-2.9}$ MPa/K at 2400 ± 200 K, respectively (Fig. 2 e-g). The location of the triple point is estimated to be ~ 22 GPa and ~ 2155 K. The probabilities of observing each phase, $\hat{p}(Y = k|P, T)$, $k = wd, rw, \text{ or } bm + pe$, are shown as a function of P with a constant T of 1800 K and 2400 K, respectively (Fig. 2a–c).

The nonlinear post-spinel boundary (more negative with increasing temperature) agrees visually with the corrected experimental data compilation (Fig. 2d). It is also in general consistent with that reported by Chanyshv et al. (2022); However, their post-spinel slope is on average slightly less negative (varies from -0.9 MPa/K at 2000 K to -0.1 MPa/K at temperatures <1700 K) and increasingly deviates from our estimate with increasing temperature. Except for Chanyshv et al. (2022), all previous studies on the post-spinel transition assumed a linear boundary and determined it with visual inspection and free-hand drawing; hence those estimates are incommensurate with the nonlinear post-spinel Clapeyron slope we reported here. Nevertheless, we performed additional tests on the literature data using the simple binary logistic model with a linear boundary for benchmarking the methodology with these previous studies. A more detailed discussion on the comparison can be found in Supplementary Text S5 and Fig. S3–5.

The $rw \leftrightarrow bm + pe$ post-spinel boundary has a considerable nonlinearity while the $wd \leftrightarrow rw$ boundary remains virtually constant over the same temperature range. This marked difference is generally consistent with the temperature- and pressure-dependent thermal expansivity trends in the Mg_2SiO_4 polymorphs, and more specifically, the divergent trends in $\Delta V_{wd \leftrightarrow rw}$ and $\Delta V_{post-spinel}$: 1) α_{rw} and α_{wd} increase at a similar rate with increasing temperature but α_{rw} increases slower than α_{bm} at high temperatures (Hernández et al., 2015); 2) the temperature-dependent thermal expansivity in rw becomes more pronounced at higher pressures (Belmonte et al., 2022). Therefore, $\Delta V_{wd \leftrightarrow rw}$ is expected to vary much less than $\Delta V_{post-spinel}$ at their relevant P – T conditions. In the meantime, the shape of the $wd \leftrightarrow bm + pe$ boundary remains underdetermined because the experimental constraints on the fields of wd and $bm + pe$ above the triple point remain sparse. Our global analysis with regularization/model selection chose a relatively simple linear boundary for the $wd \leftrightarrow bm + pe$ boundary when the data is insufficient to fit a more complex, nonlinear boundary, and it demonstrates the effectiveness of our proposed machine learning framework in avoiding overfitting.

The major limitation of all previous studies is that they focused on determining one phase boundary at a time: for example, if the primary task of the study was to determine the $rw \leftrightarrow bm + pe$ post-spinel boundary, the information contained in the phase stability observations of wd was typically ignored. The analytical methodology we proposed here concerns the exact opposite, and the task of determining the $wd \leftrightarrow rw$ and $wd \leftrightarrow bm + pe$ boundaries is not ancillary to determining the post-spinel boundary — the two tasks are one and the same. In other words, the post-spinel boundary here is statistically optimized from and consistent with the phase stability observations of all three phases/phase assemblages around the corresponding triple point, not just a simple inversion of the phase observations of rw and $bm + pe$ only.

Last but not least, our discussion is so far limited to determining the Mg_2SiO_4 phase diagram. However, this analytical methodology with multi-class logistic regression and supervised learning can be applied generally to the inversion of any phase diagram data (e.g., P – T , P – X , T – X , etc.). Many widely-used thermodynamic datasets for modeling the Earth’s mantle followed the general strategy in selecting the minimal possible set of phase stability studies that

constrain the relevant phase diagrams based on least-squares inversions (Holland & Powell, 1990; Stixrude & Lithgow-Bertelloni, 2011). Such approach is susceptible to significant errors if the experimental dataset selected *a posteriori* were systematically biased. In addition, the least-squares fits used to create the abovementioned databases are unstable with the presence of experimental outliers. Our proposed analytical methodology can get a maximum of information from all existing phase diagram data without overfitting them and is less susceptible to both systematic bias and significant outliers, which help improve our ability to directly estimate thermodynamic quantities (such as high-temperature entropy) for which experimental measurements do not exist from the relevant phase boundaries, as well as to indirectly invert other thermochemical parameters (e.g., free energy, characteristic vibrational temperature, interaction parameters).

5. Mantle expression of the nonlinear post-spinel boundary in slabs and plumes worldwide

Our understanding of how phase transition Clapeyron slopes interact with mantle flow, both upwelling and downwelling, can be briefly summarized as follows: an endothermic transition/reaction with negative Clapeyron slope (latent heat is absorbed, i.e., $\Delta H > 0$ in Equation (6) impedes the passage of mantle flow, whereas an exothermic transition/reaction with positive Clapeyron slope ($\Delta H < 0$) enhances it (e.g., Christensen, 1995). In particular, the endothermic post-spinel transition can cause localized and transient deflection to downwelling slabs and upwelling plumes. In this section, we explored the mantle expression of the nonlinearity of the post-spinel transition. First, we assembled a composite temperature map of the “660-km” discontinuity (referred to as T_{660}) that includes individual slabs and plumes across the globe as well the ambient mantle (Fig. 5a). For consistency, T_{660} is defined as the temperature at 23 GPa (slightly shallower than the depth where the post-spinel transition is expected to occur) along the adiabatic geotherm of its respective mantle potential temperature (T_p). We derived the lateral variations in T_{660} from the T_p estimates based on 2D kinematic models for subducting slabs (Syracuse et al., 2010), global shear velocity constraints for plume-fed hotspots (Bao et al., 2022), and globally compiled S660S observations for the ambient mantle (Waszek et al., 2021). Further details of this composite T_{660} model can be found in Supplementary Text S6. The mantle temperature variation patterns in these three independently-constrained thermal models are consistent with each other; for example, mantle temperature is the lowest around the Western Pacific subduction zones while the plume-fed hotspots coincide with the positive T_{660} anomalies in the ambient mantle.

The ambient mantle has a global average T_{660} of 1955 ± 74 K (one standard deviation, same hereafter). The post-spinel transition is the predominant *bm*-forming reaction when T_{660} is between 1400 K and 2050 K near 23 GPa (Stixrude & Lithgow-Bertelloni, 2011). The “660-km” seismic discontinuity coincides with the post-spinel transition, and it contains the sharpest changes in seismic properties. Equally significant changes in temperature, rheology, and buoyancy are also accompanied by the post-spinel transition. The Clapeyron slope of the post-

spinel transition, $\gamma_{\text{post-spinel}}$, hence, becomes one of the most important constraints on mantle convection.

A nonlinear post-spinel transition means that its Clapeyron slope is temperature dependent. To visualize this, we produced a global map of post-spinel Clapeyron slope at the “660-km” discontinuity (Fig. 5b) based on the composite T_{660} map where the post-spinel transition is predominant (Fig. 5a). The ambient mantle has a global average $\gamma_{\text{post-spinel}}$ of -3.1 ± 0.6 MPa/K ($\sim 91\%$ of the total surface of the “660-km” layer), which is consistent with the seismically derived post-spinel Clapeyron slope of ~ -3 MPa/K for the ambient mantle structure of the western half of the continental U.S. (Tauzin & Ricard, 2014). The slabs accompanied by the post-spinel transition have an average T_{660} of 1569 ± 125 K and an average $\gamma_{\text{post-spinel}}$ of -0.9 ± 0.5 MPa/K (45 of 50 slabs considered here), while the hotspot-associated plumes have an average T_{660} of 2030 ± 71 K and an average $\gamma_{\text{post-spinel}}$ slope of -3.3 ± 0.6 MPa/K (5 of 26 plume-fed hotspots considered here). We found that the post-spinel Clapeyron slopes associated with the plumes (upwelling) are nearly three times more negative than those associated with the slabs (downwelling).

The temperature-dependent post-spinel Clapeyron slope renders a varying degree of hindrance to subducting slabs. Qualitatively speaking, the majority of the subducting slabs are cold (mostly clustered around the West Pacific with $T_{660} = 1400\text{--}1600$ K) and have a slightly negative post-spinel Clapeyron slope of $-0.6\text{--}0.7$ MPa/K; these cold slabs are expected to encounter little to moderate hinderance from the post-spinel transition across the “660-km” depth. On the contrary, several hot slabs near Colombia/Ecuador ($T_{660} = \sim 1810$ K), Central Cascadia ($T_{660} = \sim 1880$ K), and North Cascadia ($T_{660} = \sim 1930$ K) have much more negative post-spinel Clapeyron slopes of $-1.8\text{--}2.9$ MPa/K and are expected to encounter much greater hinderance to subduction from the post-spinel transition. We caution that any quantitative interpretation of the observed morphologies of subducting slabs must take into account other factors including (1) the viscosity and/or compositional contrasts between the upper and lower mantle and (2) the configuration and subduction history of the specific subduction zone (e.g., shape, strength trench motion) (e.g., Goes et al., 2017). Therefore, we advocate a reassessment of global subduction zone dynamics with the temperature-dependent post-spinel Clapeyron slope, which would help elucidate the diverse range of observed slab morphologies: some slabs remain neutrally buoyant temporarily (stagnation) at the base of the transition zone while others penetrate the lower mantle. Furthermore, if we consider the temporal evolution of one single slab, the effects of rheology and buoyancy driven by the temperature-dependent post-spinel transition may vary its dynamics and morphology over its lifetime as the slab becomes thermally equilibrated with the surrounding ambient mantle.

For the hotspot-associated mantle plumes accompanied primarily by the post-spinel transition near the “660-km” depth ($T_{660} = 1870\text{--}2050$ K in the compilation of global volcanic hotspots by Bao et al., 2022, 5 plumes in total considered here), the post-spinel Clapeyron slope is estimated to range from -2.5 MPa/K at $T_{660} = 1890$ K (Ascension) to -3.8 MPa/K at $T_{660} = 2010$ K (Cape Verde). According to geodynamic modeling (e.g., Bossmann & van Keken, 2013),

the post-spinel transition tends to trap plume heads at $\gamma = < \sim -3.4$ MPa/K while plumes ascend into the upper mantle at $\gamma = > \sim -2.8$ MPa/K; ring-shaped secondary plumes may form when γ is between -3.4 and -2.8 MPa/K. Therefore, the “660 km” depth is expected to hinder the passage of three post-spinel dominated plumes, Cameroon ($\gamma_{\text{post-spinel}} = -3.5$ MPa/K at $T_{660} = \sim 1980$ K), Crozet ($\gamma_{\text{post-spinel}} = -3.6$ MPa/K at $T_{660} = \sim 1995$ K), and Cape Verde ($\gamma_{\text{post-spinel}} = -3.8$ MPa/K at $T_{660} = \sim 2010$ K); while the plumes in two locations, Ascension ($\gamma_{\text{post-spinel}} = -2.5$ MPa/K at $T_{660} = \sim 1890$ K) and Manus Basin ($\gamma_{\text{post-spinel}} = -2.8$ MPa/K at $T_{660} = \sim 1920$ K), ascend across the “660 km” depth without much impediment. In addition, the dynamic topography of large igneous provinces above the post-spinel dominated plumes is influenced by $\gamma_{\text{post-spinel}}$ and can be used to estimate the T_{660} : the dynamic subsidence decreases and lasts shorter as γ becomes more positive, from 100 m and 14 Ma at $\gamma = -3.0$ MPa/K to 200 m and 20 Ma at $\gamma = -3.2$ MPa/K (Leng & Zhong, 2010), and such change in surface subsidence can be attributed to a difference of 20 K in mantle temperature (from 1940 to 1960 K).

If the Earth’s mantle is made of the simplified Mg_2SiO_4 system only, a *bm*-forming reaction, $wd \leftrightarrow bm + pe$ with the Clapeyron slope of ~ 0 MPa/K, would replace the post-spinel transition when T_{660} is above ~ 2155 K (above the *wd-rw-bm/pe* triple point). In a more realistic mantle composition (e.g., pyrolite), however, *wd* becomes increasingly less stable than majorite garnet (*gt*) (Stixrude & Lithgow-Bertelloni, 2011). The post-garnet transition, $gt \leftrightarrow bm$, rather than the post-spinel transition or the $wd \leftrightarrow bm + pe$ transition, is expected to dominate some hotspot locations (hatched symbols in Fig. 5b) where T_{660} is above ~ 2050 K (Stixrude & Lithgow-Bertelloni, 2011), such as the Eastern and Southern Pacific; it is expected to affect less than $\sim 2\%$ of the total surface of the “660-km” depth of the ambient mantle (hatched areas in Fig. 5b, the areal fraction distorted visually due to projection). This post-garnet transition is analogous to the one in the MgSiO_3 system and displays a positive Clapeyron slope of 1–4 MPa/K (e.g., Hirose, 2002, Ishii et al., 2011), with opposite sign to the post-spinel transition; the magnitude of the post-garnet Clapeyron slope currently remains underdetermined by existing experimental constraints.

Another *bm*-forming reaction, akimotoite (*ak*) $\leftrightarrow bm$ may replace the post-spinel transition in a small number of extremely cold slabs when T_{660} is below 1400 K, such as Tonga ($T_{660} = \sim 1320$ K) as well as Kamchatka, Kurile, and West Banda Sea ($T_{660} = \sim 1380$ K). The presence of $ak \leftrightarrow bm$ has been seismically observed in the coldest Tonga slab. The $rw \leftrightarrow ak + pe$ transition in Mg_2SiO_4 is nearly identical to the same transition in pyrolite and has a negative Clapeyron slope of -8.1 MPa/K at low temperatures up to 1300 K (Chanyshev et al., 2022) and hence significantly hinder the passage of subducting slabs towards the lower mantle. The extremely cold condition for the $ak \leftrightarrow bm$ transition is unlikely to be present in the ambient mantle today based on our temperature estimates.

The global map of lateral variations in the post-spinel Clapeyron slope along with the identified regions of the post-garnet and $rw \leftrightarrow ak + pe$ transitions provides a spatial guide for us to study subducting slabs and hotspot-associated plumes worldwide (buoyancy-driven, active upwelling and downwelling) in their specific Clapeyron slope magnitude. In addition, the

temperature-dependent post-spinel Clapeyron slope also permits a varying degree of convective layering and hence an evolving temperature contrast across the “660-km” depth through time. These nonlinear effects ultimately depend on T_{660} and remain virtually unexplored in geodynamical models. It is therefore critical to model the thermal and dynamical evolution of slabs, plumes and the ambient mantle consistent with the temperature-dependent post-spinel Clapeyron slope.

6 Conclusions

The phase diagrams of mantle minerals have been investigated experimentally in the past several decades thanks to developments in high pressure techniques. Of these, the Mg_2SiO_4 phase diagram is the most extensively studied, because the Clapeyron slope of its post-spinel boundary represents one of the most important constraints on mantle dynamics. Yet the existing experimental datasets on the Mg_2SiO_4 phase diagram still show notable discrepancies in the location and Clapeyron slope of the post-spinel transition as well as the triple point of wd , rw , and $bm + pe$. The lack of rigorous analysis on inter-run and inter-lab uncertainties in the experimental results has motivated us to develop a machine learning framework with multi-class logistical regression and supervised learning algorithms for the determination of high-pressure phase diagrams. As a proof of concept, we have applied such analytical methodology to the Mg_2SiO_4 phase diagram data, including the new dataset reported by this study and previously-published datasets with redetermined P and T . Among our findings are that the post-spinel Clapeyron slope varies locally from $-2.3^{+0.6}_{-1.4}$ MPa/K at 1900 ± 50 K, to $-1.0^{+1.3}_{-1.7}$ MPa/K at 1700 ± 50 K, and to $0.0^{+1.7}_{-2.0}$ MPa/K at 1500 ± 50 K and that the location of the triple point is statistically optimized at ~ 22 GPa and ~ 2155 K. Our proposed analytical methodology with machine learning can be applied generally for data inversion in phase diagram data and provides a tool to accurately predict thermodynamic modeling parameters.

Most importantly, the polymorphic phase transitions and solid-state reactions in Mg_2SiO_4 have been historically conceived to be linear, but we found that the post-spinel boundary is noticeably nonlinear and its Clapeyron slope temperature dependent. To explore the mantle expression of the nonlinearity, we first presented a composite temperature map of the “660-km” discontinuity with which the post-spinel transition coincides and then estimated the lateral variation of the post-spinel Clapeyron slope, in subducting slabs and hotpot-associated plumes worldwide, as well as most of the ambient mantle. The nonlinearity of the post-spinel transition shifts our conceptual scheme of its role in mantle convection: its geodynamical effects are temperature dependent and the existing models of mantle flow across the “660-km” discontinuity, both upwelling and downwelling, need to be reassessed with the temperature-dependent Clapeyron slope.

Acknowledgments

J. Dong was supported by a James Mills Peirce Fellowship from the Graduate School of Arts and Sciences at Harvard University. R. A. Fischer was supported by the Henry Luce Foundation. L.P. Stixrude was supported by the National Science Foundation (EAR-1853388). M.C. Brennan was supported by a National Science Foundation Graduate Research Fellowship (DGE-1745303). We thank Andrew J. Campbell for loaning us the use of his short symmetric cell for a portion of these gas membrane experiments. The experimental part of this work was performed at GeoSoilEnviroCARS (Sector 13) and HPCAT (Sector 16), Advanced Photon Source (APS), Argonne National Laboratory. The Advanced Photon Source is a U.S. Department of Energy (DOE) Office of Science User Facility operated for the DOE Office of Science by Argonne National Laboratory under Contract No. DE-AC02-06CH11357. GeoSoilEnviroCARS is supported by the National Science Foundation (EAR – 1634415) and DOE (DE-FG02-94ER14466). HPCAT operations are supported by the National Nuclear Security Administration (DOE-NNSA)'s Office of Experimental Sciences. The data analysis part of this work was inspired by a Harvard class, CS109a: Introduction to Data Science, taught by Pavlos Protopapas, Kevin A. Rader, and Chris Tanner in Fall 2020, and this work benefited from its course materials.

Data Availability Statement

The experimental datasets on phase stability in Mg_2SiO_4 used in this study are available in Tables S1–S3 within the supporting information, or within the Zenodo repository (located via <https://doi.org/10.5281/zenodo.7007673>).

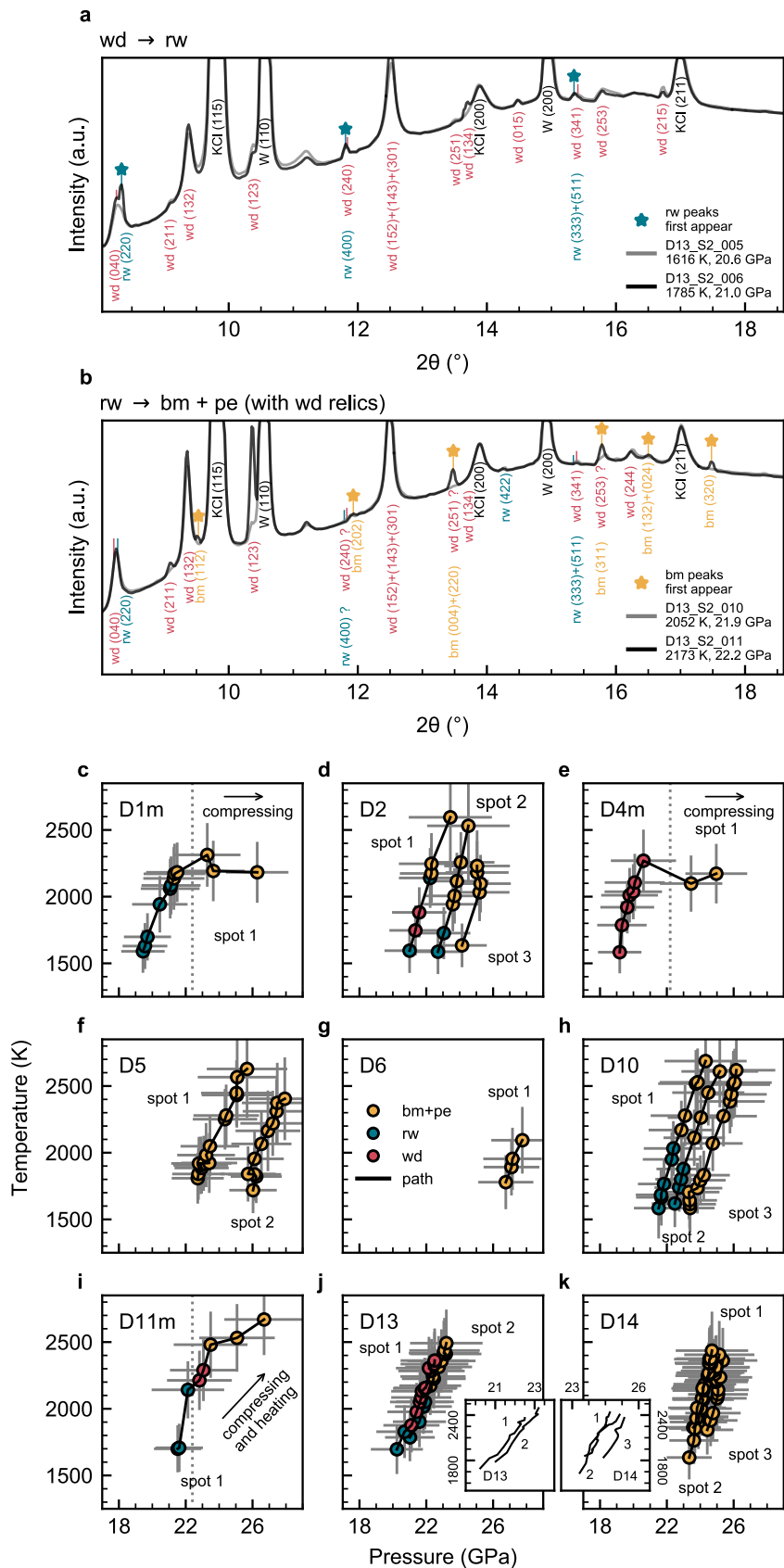


Figure 1: In situ phase stability observations in Mg_2SiO_4 collected in LH-DAC experiments with synchrotron XRD from this study. (a–b) Representative diffraction patterns from run D13 demonstrating the first appearance of the peaks of a new phase (marked by colored stars), from wd to rw (a), and then from rw to bm (+ pe) (b). All visible diffraction peaks of D13_S2_005 can be attributed to wd , including prominent peaks (040), (132), (152), (143), and (301), and minor peaks (211), (123), (240), (251) (?), (015), (341), (253), and (215), and wd is the only stable phase at 1616 K, 20.6 GPa. In D13_S2_006, the rw peaks appeared for the first time, (220), (400), and (341), and wd began transforming into rw at 1785 K, 21.0 GPa. The rw peaks of D13_S2_010 at 2052 K, 21.9 GPa continued to grow from D13_S2_006 at 1785 K, 21.0 GPa but became increasingly overlapped with the wd peaks at high temperatures (e.g., wd (040) and rw (220)). In D13_S2_011, the bm peaks appeared for the first time (112), (202), (311), (132), (024), and (320), and rw began transforming into bm (+ pe) at 2173 K, 22.2 GPa. All peaks are identified and labeled by (hkl) . (c–k) P – T paths of phase stability observations in each experimental run (solid black line) with uncertainties (grey crosses). Phases are color coded as follow: wd in red, rw in blue, bm + pe in yellow.

1

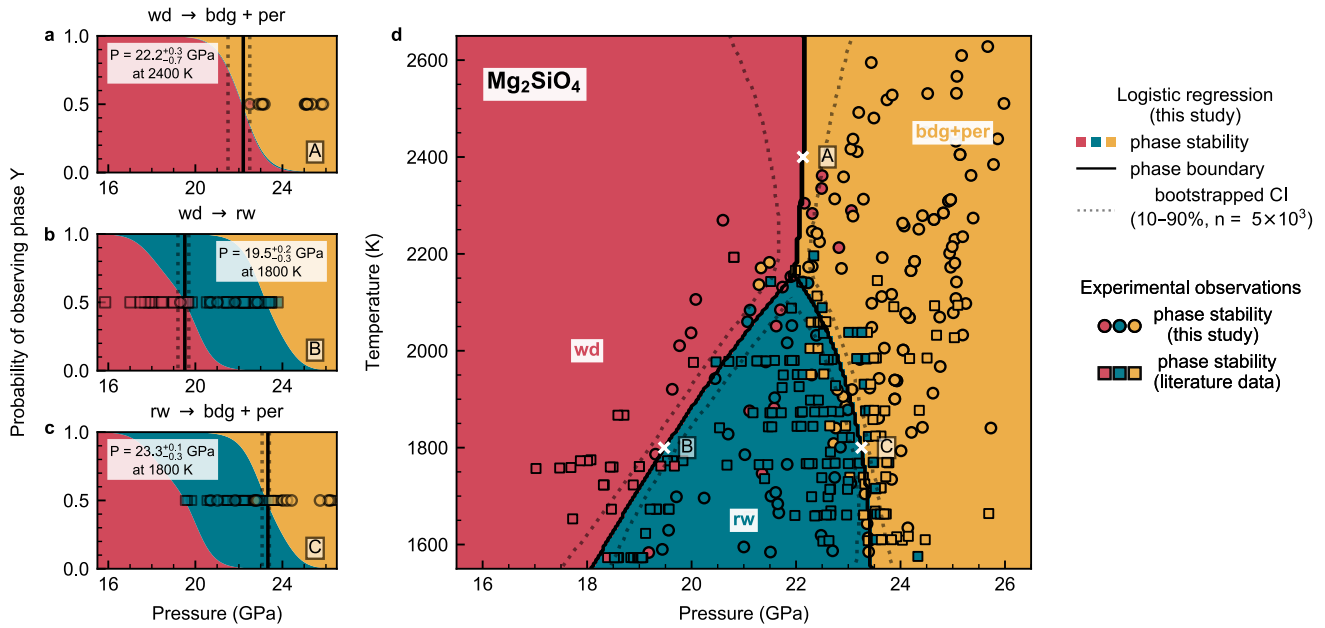


Figure 2: Machine learned phase diagram of Mg_2SiO_4 at transition zone conditions. (a–c) Probabilities of observing the (a) $wd \leftrightarrow bm + pe$, (b) $wd \leftrightarrow rw$, and (c) $rw \leftrightarrow bm + pe$ phase transition are predicted at (a) 2400 K and (b–c) 1800 K, respectively, with multiple logistic regression and supervised learning algorithms. Experimental observations made within 100 K of those prediction temperatures are shown with the predicted probability curves in (a–c). The phase transition pressure at the prediction temperature is the vertical solid line in each plot with uncertainties in the vertical grey dashed lines. (d) Phase stability fields of wd , rw and $bm + pe$ are predicted between 1500 and 2700 K and between 15 and 27 GPa with a bootstrapped confidence interval (CI) of 10–90% in the grey dashed lines. Experimental observations (circles: this study; squares: literature data) are shown with the predicted phase stability fields. $P-T$ conditions for (a–c) are indicated by point A, B and C in (d) with a white cross. Phases are color coded as follow: wd in red, rw in blue, and $bm + pe$ in yellow.

2

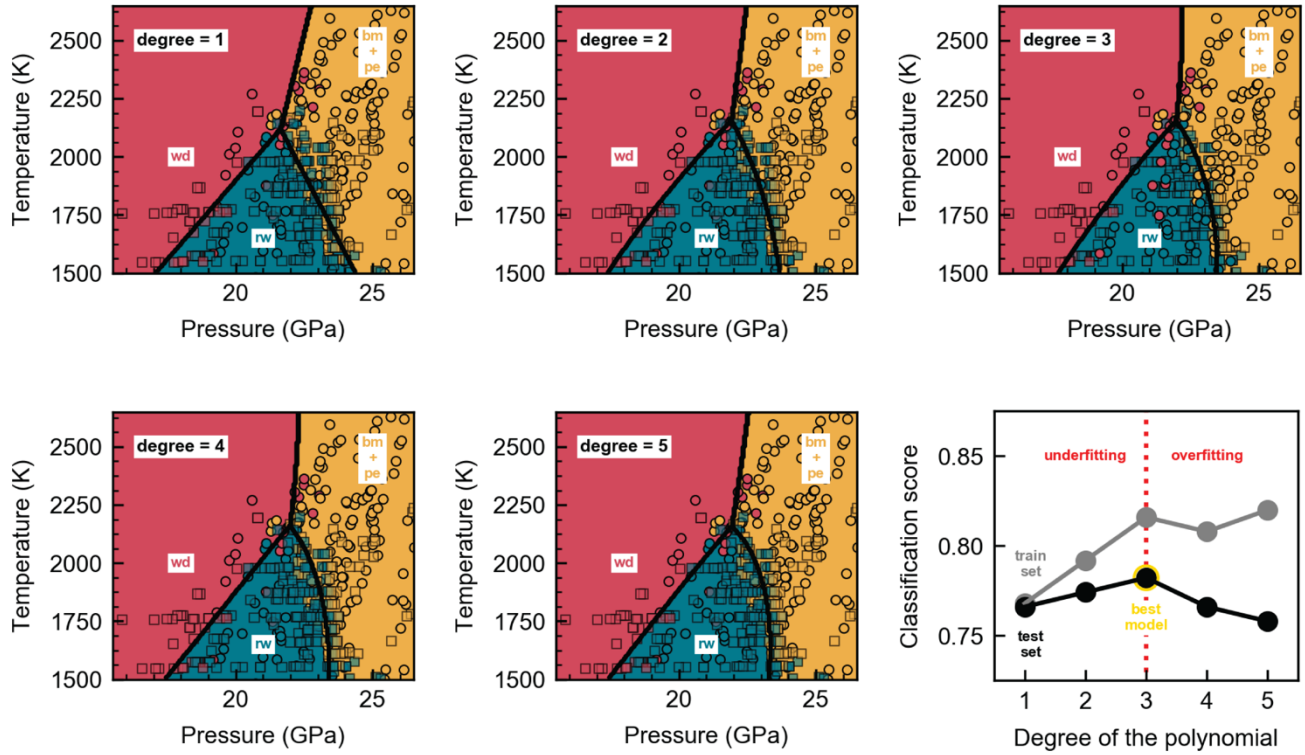


Figure 3: Model selection and evaluation for the Mg_2SiO_4 phase diagram. (a–e) Hyperparameter optimized predictions for phase stability fields of *wd*, *rw* and *bm + pe* with different degree of polynomial functions ($n = 1–5$) using multi-class logistic model and supervised learning. Legend is the same as in Figure 2. (f) Model performance (bias and variance measured by F_1 score) as a function of degree of polynomials. As the degree of the polynomial function increases, the performance of the model over the train set (solid grey circles) increases continuously. On the other hand, the performance over the test set (solid black circles) increases initially but after degree 2 ($n = 3$), the classification score of the test set starts to decrease. Among the degree of the polynomial ($n = 1–5$) we tested in the study, $n = 3$ (highlighted in gold) is selected as the best parameter to balance the bias-variance trade-off in the model.

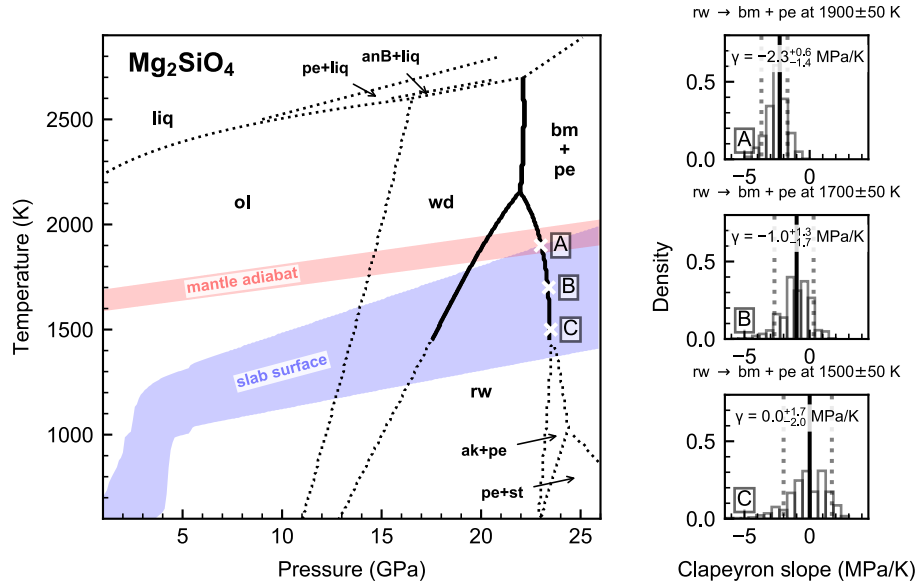


Figure 4: Temperature-dependent Clapeyron slope in the post-spinel transition in Mg_2SiO_4 . (a) Phase diagram for Mg_2SiO_4 up to 26 GPa. Three phase boundaries, $wd \leftrightarrow rw$, $wd \leftrightarrow bm + pe$, and $rw \leftrightarrow bm + pe$, at the transition zone conditions are statistically optimized from this study (solid black lines). The melting boundaries and the $ol \leftrightarrow wd$, $ak \leftrightarrow bm$, and $pe + st \leftrightarrow bm$ (dashed black lines) are adapted from Li (2022) and Stixrude & Lithgow-Bertelloni (2022), respectively. (b–d) The distributions of the estimated Clapeyron slopes of the $rw \leftrightarrow bm + pe$ post-spinel transition at (b) 1900 K, (c) 1700 K, and (d) 1500 K are produced with bootstrap resampling ($n = 5 \times 10^3$), and the local Clapeyron slope for the post-spinel transition is averaged within 50 K of its prediction temperatures (in the vertical solid line in each plot) with a bootstrapped confidence interval (CI) of 10–90% in the vertical grey dashed lines. P – T conditions for (b–d) are indicated by point A, B and C in (a) with a cross. The present-day ambient mantle adiabats were estimated based on Stixrude & Lithgow-Bertelloni (2011) with mantle potential temperatures between 1550–1650 K. The slab surface temperatures were extrapolated from a global compilation of subduction zone thermal models reported by Syracuse et al. (2010).

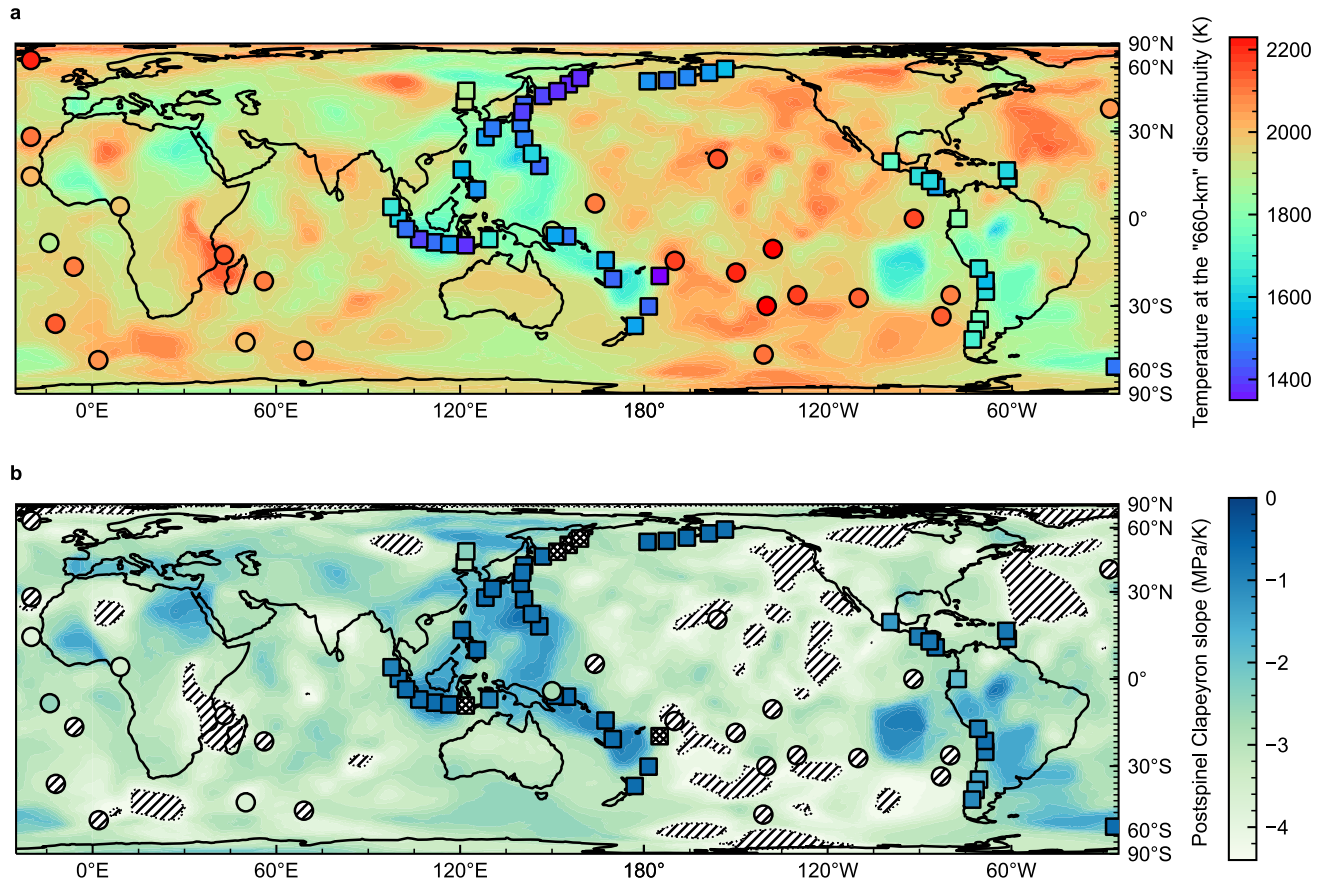


Figure 5: Global mapping of mantle temperature and post-spinel Clapeyron slope at the “660-km” discontinuity with superimposed subducting slabs and plume-fed hotspots locations. (a) Composite temperature map of the “660-km” discontinuity for ambient mantle (color-coded background, based on globally compiled S660S observations from Waszek et al. (2021)), subducting slabs (color-coded square, based on 2D kinematic models from Syracuse et al. (2010)) and plume-fed hotspots (color-coded circle, based on global shear velocity constraints from Bao et al. (2022)). The temperature variation patterns in these three independently constrained thermal models are consistent with each other; for example, temperature is the lowest around the Western Pacific subduction zones while the plume-fed hotspots coincide with the positive T_{660} anomalies in the ambient mantle. **(b)** Composite post-spinel Clapeyron slope map of the “660-km” discontinuity based on the nonlinearity of the post-spinel transition (Fig. 4 and Fig. S5 from this study). A more negative post-spinel Clapeyron slope would produce stronger hindrance to the passage of mantle flow, both upwelling and downwelling. The subducting slabs (colored square) and plume-fed hotspots (colored circle) dominated by the post-spinel transition are color-coded based on the magnitude of Clapeyron slope, while those dominated by the $rw \leftrightarrow ak + pe$ transition (<1400 K in slabs) and post-garnet transition (>2050 K in plumes) are highlighted with hatched square and circle, respectively. Lateral variations of the post-spinel Clapeyron slope at the “660-km” discontinuity in the ambient mantle are shown as the color-coded background, and the potential regions of the ambient mantle influenced by the post-garnet transition (>2050 K) are hatched and outlined in thin dotted black lines. The name and location of each subducting slabs or plume-fed hotspot are listed with its post-spinel Clapeyron slope in Table S5–S6.

8 **References:**

- 9
- 10 Ballmer, M. D., Schmerr, N. C., Nakagawa, T., & Ritsema, J. (2015). Compositional mantle layering
11 revealed by slab stagnation at ~1000-km depth. *Science Advances*, *1*(11), e1500815.
12 <https://doi.org/10.1126/sciadv.1500815>
- 13 Bao, X., Lithgow-Bertelloni, C. R., Jackson, M. G., & Romanowicz, B. (2022). On the relative
14 temperatures of Earth's volcanic hotspots and mid-ocean ridges. *Science*, *375*, 57–61.
15 <https://doi.org/http://dx.doi.org/10.1126/science.abj8944>
- 16 Belmonte, D., la Fortezza, M., & Menescardi, F. (2022). Ab initio thermal expansion and thermoelastic
17 properties of ringwoodite (γ -Mg₂SiO₄) at mantle transition zone conditions. *European Journal of*
18 *Mineralogy*, *34*(2), 167–182. <https://doi.org/10.5194/ejm-34-167-2022>
- 19 Bishop, C. M. (2006). *Pattern Recognition and Machine Learning* (M. Jordan, J. Kleinberg, & B.
20 Schölkopf, Eds.). Springer.
- 21 Bossmann, A. B., & van Keken, P. E. (2013). Dynamics of plumes in a compressible mantle with phase
22 changes: Implications for phase boundary topography. *Physics of the Earth and Planetary*
23 *Interiors*, *224*, 21–31. <https://doi.org/10.1016/j.pepi.2013.09.002>
- 24 Campbell, A. J., Danielson, L., Richter, K., Seagle, C. T., Wang, Y., & Prakapenka, V. B. (2009). High
25 pressure effects on the iron-iron oxide and nickel-nickel oxide oxygen fugacity buffers. *Earth and*
26 *Planetary Science Letters*, *286*(3–4), 556–564. <https://doi.org/10.1016/j.epsl.2009.07.022>
- 27 Chanyshev, A., Ishii, T., Bondar, D., Bhat, S., Kim, E. J., Farla, R., Nishida, K., Liu, Z., Wang, L.,
28 Nakajima, A., Yan, B., Tang, H., Chen, Z., Higo, Y., Tange, Y., & Katsura, T. (2022). Depressed
29 660-km discontinuity caused by akimotoite–bridgmanite transition. *Nature*, *601*(7891), 69–73.
30 <https://doi.org/10.1038/s41586-021-04157-z>
- 31 Christensen, U. (1995). Effects of Phase Transitions on Mantle Convection. *Annual Review of Earth and*
32 *Planetary Sciences*, *23*, 65–87.
33 <https://doi.org/https://doi.org/10.1146/annurev.ea.23.050195.000433>
- 34 Chudinovskikh, L., & Boehler, R. (2001). High-pressure polymorphs of olivine and the 660-km seismic
35 discontinuity. *Nature*, *411*, 574–577. <https://doi.org/10.1038/35079060>
- 36 Deuss, A., Andrews, J., & Day, E. (2013). Seismic Observations of Mantle Discontinuities and Their
37 Mineralogical and Dynamical Interpretation. In *Physics and Chemistry of the Deep Earth* (pp. 295–
38 323). John Wiley and Sons. <https://doi.org/10.1002/9781118529492.ch10>
- 39 Fabrichnaya, O. (2008). Calculation of the phase diagrams of the MgO–FeO–Al₂O₃–SiO₂ system at
40 high pressures and temperatures: application to the mineral structure of the Earth's mantle
41 transition zone. In K. Hack (Ed.), *The SGTE Casebook: Thermodynamics at Work* (Second Edition,
42 pp. 132–143). Woodhead Publishing. <https://doi.org/https://doi.org/10.1533/9781845693954.2.132>
- 43 Fei, Y., Ricolleau, A., Frank, M., Mibe, K., Shen, G., & Prakapenka, V. (2007). Toward an internally
44 consistent pressure scale. *Proceedings of the National Academy of Sciences*, *104*(22), 9182–9186.
45 <https://www.pnas.org>
- 46 Fei, Y., van Orman, J., Li, J., van Westrenen, W., Sanloup, C., Minarik, W., Hirose, K., Komabayashi,
47 T., Walter, M., & Funakoshi, K. (2004). Experimentally determined postspinel transformation
48 boundary in Mg₂SiO₄ using MgO as an internal pressure standard and its geophysical
49 implications. *Journal of Geophysical Research: Solid Earth*, *109*(B2).
50 <https://doi.org/10.1029/2003jb002562>
- 51 Ghosh, S., Ohtani, E., Litasov, K. D., Suzuki, A., Dobson, D., & Funakoshi, K. (2013). Effect of water
52 in depleted mantle on post-spinel transition and implication for 660km seismic discontinuity. *Earth*
53 *and Planetary Science Letters*, *371–372*, 103–111. <https://doi.org/10.1016/j.epsl.2013.04.011>

54 Hernández, E. R., Brodholt, J., & Alfè, D. (2015). Structural, vibrational and thermodynamic properties
55 of Mg₂SiO₄ and MgSiO₃ minerals from first-principles simulations. *Physics of the Earth and*
56 *Planetary Interiors*, 240, 1–24. <https://doi.org/10.1016/j.pepi.2014.10.007>

57 Hirose, K. (2002). Phase transitions in pyrolitic mantle around 670-km depth: Implications for upwelling
58 of plumes from the lower mantle. *Journal of Geophysical Research: Solid Earth*, 107(B4), ECV 3-
59 1-ECV 3-13. <https://doi.org/10.1029/2001jb000597>

60 Holland, T. J. B., & Powell, R. (1990). An enlarged and updated internally consistent thermodynamic
61 dataset with uncertainties and correlations: the system K₂O-Na₂O-CaO-MgO-MnO-FeO-Fe₂O₃-
62 Al₂O₃-TiO₂-SiO₂-C-H₂-O₂. In *metamorphic Ceol* (Vol. 0).
63 <https://doi.org/https://doi.org/10.1111/j.1525-1314.1990.tb00458.x>

64 Inoue, T., Irifune, T., Higo, Y., Sanehira, T., Sueda, Y., Yamada, A., Shinmei, T., Yamazaki, D., Ando,
65 J., Funakoshi, K., & Utsumi, W. (2006). The phase boundary between wadsleyite and ringwoodite
66 in Mg₂ SiO₄ determined by in situ X-ray diffraction. *Physics and Chemistry of Minerals*, 33(2),
67 106–114. <https://doi.org/10.1007/s00269-005-0053-y>

68 Irifune, T., Nishiyama, N., Kuroda, K., Inoue, T., Isshiki, M., Utsumi, W., Urakawa, S., Uchida, T., &
69 Ohtaka, O. (1998). The Postspinel Phase Boundary in Mg₂SiO₄ Determined by in Situ X-ray
70 Diffraction. *Science*, 279(5357), 1698–1700. <https://doi.org/10.1126/science.279.5357.1698>

71 Ishii, T., Huang, R., Myhill, R., Fei, H., Koemets, I., Liu, Z., Maeda, F., Yuan, L., Wang, L., Druzhbin,
72 D., Yamamoto, T., Bhat, S., Farla, R., Kawazoe, T., Tsujino, N., Kulik, E., Higo, Y., Tange, Y., &
73 Katsura, T. (2019). Sharp 660-km discontinuity controlled by extremely narrow binary post-spinel
74 transition. *Nature Geoscience*, 12(10), 869–872. <https://doi.org/10.1038/s41561-019-0452-1>

75 Ishii, T., Kojitani, H., & Akaogi, M. (2011). Post-spinel transitions in pyrolite and Mg₂SiO₄ and
76 akimotoite-perovskite transition in MgSiO₃: Precise comparison by high-pressure high-temperature
77 experiments with multi-sample cell technique. *Earth and Planetary Science Letters*, 309(3–4), 185–
78 197. <https://doi.org/10.1016/j.epsl.2011.06.023>

79 Ito, E., & Takahashi, E. (1989). Postspinel transformations in the system Mg₂SiO₄-Fe₂SiO₄ and some
80 geophysical implications. *Journal of Geophysical Research*, 94(B8).
81 <https://doi.org/10.1029/jb094ib08p10637>

82 James, G., Witten, D., Hastie, T., & Tibshirani, R. (2013). *An Introduction to Statistical Learning* (G.
83 Casella, S. Fienberg, & I. Olkin, Eds.). Springer. <http://www.springer.com/series/417>

84 Katsura, T., Yamada, H., Shinmei, T., Kubo, A., Ono, S., Kanzaki, M., Yoneda, A., Walter, M. J., Ito,
85 E., Urakawa, S., Funakoshi, K., & Utsumi, W. (2003). Post-spinel transition in Mg₂SiO₄
86 determined by high P - T in situ X-ray diffractometry. *Physics of the Earth and Planetary Interiors*,
87 136(1–2), 11–24. [https://doi.org/10.1016/S0031-9201\(03\)00019-0](https://doi.org/10.1016/S0031-9201(03)00019-0)

88 Kavner, A., & Jeanloz, R. (1998). High-pressure melting curve of platinum. *Journal of Applied Physics*,
89 83(12), 7553–7559. <https://doi.org/10.1063/1.367520>

90 Kavner, A., Speed, T., & Jeanloz, R. (2011). Statistical Analysis of Phase-Boundary Observations. In
91 *Physics Meets Mineralogy* (pp. 71–80). Cambridge University Press.
92 <https://doi.org/10.1017/cbo9780511896590.006>

93 Kojitani, H., Inoue, T., & Akaogi, M. (2016). Precise measurements of enthalpy of postspinel transition
94 in Mg₂SiO₄ and application to the phase boundary calculation. *Journal of Geophysical Research:*
95 *Solid Earth*, 121(2), 729–742. <https://doi.org/10.1002/2015JB012211>

96 Kojitani, H., Terata, S., Ohsawa, M., Mori, D., Inaguma, Y., & Akaogi, M. (2017). Experimental and
97 thermodynamic investigations on the stability of Mg₁₄Si₅O₂₄ anhydrous phase B with relevance
98 to Mg₂SiO₄ forsterite, wadsleyite, and ringwoodite. *American Mineralogist*, 102(10), 2032–2044.
99 <https://doi.org/10.2138/am-2017-6115>

100 Leng, W., & Zhong, S. (2010). Surface subsidence caused by mantle plumes and volcanic loading in
101 large igneous provinces. *Earth and Planetary Science Letters*, 291(1–4), 207–214.
102 <https://doi.org/10.1016/j.epsl.2010.01.015>

103 Li, J. (2022). Synthesis of high-pressure silicate polymorphs using multi-anvil press. In Y. Fei & M. J.
104 Walter (Eds.), *Static and Dynamic High Pressure Mineral Physics*. Cambridge University Press.

105 Litasov, K. D., Gavryushkin, P. N., Dorogokupets, P. I., Sharygin, I. S., Shatskiy, A., Fei, Y.,
106 Rashchenko, S. v., Seryotkin, Y. v., Higo, Y., Funakoshi, K., & Ohtani, E. (2013). Thermal
107 equation of state to 33.5 GPa and 1673 K and thermodynamic properties of tungsten. *Journal of*
108 *Applied Physics*, 113(13). <https://doi.org/10.1063/1.4799018>

109 Meng, Y., Hrubciak, R., Rod, E., Boehler, R., & Shen, G. (2015). New developments in laser-heated
110 diamond anvil cell with in situ synchrotron x-ray diffraction at High Pressure Collaborative Access
111 Team. *Review of Scientific Instruments*, 86(7). <https://doi.org/10.1063/1.4926895>

112 Pedregosa, F., Varoquaux, G., Gramfort, A., Michel, V., Thirion, B., Grisel, O., Blondel, M.,
113 Prettenhofer, P., Weiss, R., Bubourg, V., Vanderplas, J., Passos, A., Cournapeau, D., Brucher, M.,
114 Perrot, M., & Duchesnay, É. (2011). Scikit-learn: Machine Learning in Python. *Journal of Machine*
115 *Learning Research*, 12, 2825–2830. <http://scikit-learn.sourceforge.net>.

116 Prakapenka, V. B., Kubo, A., Kuznetsov, A., Laskin, A., Shkurikhin, O., Dera, P., Rivers, M. L., &
117 Sutton, S. R. (2008). Advanced flat top laser heating system for high pressure research at
118 GSECARS: Application to the melting behavior of germanium. *High Pressure Research*, 28(3),
119 225–235. <https://doi.org/10.1080/08957950802050718>

120 Shim, S.-H., Duffy, T. S., & Shen, G. (2001). The post-spinel transformation in Mg₂SiO₄ and its
121 relation to the 660-km seismic discontinuity. *Nature*, 411, 571–574.
122 <https://doi.org/10.1038/35079053>

123 Sokolova, T. S., Dorogokupets, P. I., Dymshits, A. M., Danilov, B. S., & Litasov, K. D. (2016).
124 Microsoft excel spreadsheets for calculation of P–V–T relations and thermodynamic properties
125 from equations of state of MgO, diamond and nine metals as pressure markers in high-pressure and
126 high-temperature experiments. *Computers and Geosciences*, 94, 162–169.
127 <https://doi.org/10.1016/j.cageo.2016.06.002>

128 Stixrude, L., & Lithgow-Bertelloni, C. (2011). Thermodynamics of mantle minerals - II. Phase
129 equilibria. *Geophysical Journal International*, 184(3), 1180–1213. [https://doi.org/10.1111/j.1365-](https://doi.org/10.1111/j.1365-246X.2010.04890.x)
130 [246X.2010.04890.x](https://doi.org/10.1111/j.1365-246X.2010.04890.x)

131 Stixrude, L., & Lithgow-Bertelloni, C. (2022). Thermal expansivity, heat capacity and bulk modulus of
132 the mantle. *Geophysical Journal International*, 228(2), 1119–1149.
133 <https://doi.org/10.1093/gji/ggab394>

134 Suzuki, A., Ohtani, E., Morishima, H., Kubo, T., Kanbe, Y., Kondo, T., Okada, T., Terasaki, H., Kato,
135 T., & Kikegawa, T. (2000). In situ determination of the phase boundary between wadsleyite and
136 ringwoodite in Mg₂SiO₄. *Geophysical Research Letters*, 27(6), 803–806.
137 <https://doi.org/10.1029/1999GL008425>

138 Syracuse, E. M., van Keken, P. E., Abers, G. A., Suetsugu, D., Bina, C., Inoue, T., Wiens, D., &
139 Jellinek, M. (2010). The global range of subduction zone thermal models. *Physics of the Earth and*
140 *Planetary Interiors*, 183(1–2), 73–90. <https://doi.org/10.1016/j.pepi.2010.02.004>

141 Tateno, S., Komabayashi, T., Hirose, K., Hirao, N., & Ohishi, Y. (2019). Static compression of B2 KCl
142 to 230 GPa and its P–V–T equation of state. *American Mineralogist*, 104(5), 718–723.
143 <https://doi.org/10.2138/am-2019-6779>

- 144 Tauzin, B., & Ricard, Y. (2014). Seismically deduced thermodynamics phase diagrams for the mantle
145 transition zone. *Earth and Planetary Science Letters*, *401*, 337–346.
146 <https://doi.org/10.1016/j.epsl.2014.05.039>
- 147 Waszek, L., Tauzin, B., Schmerr, N. C., Ballmer, M. D., & Afonso, J. C. (2021). A poorly mixed mantle
148 transition zone and its thermal state inferred from seismic waves. *Nature Geoscience*, *14*(12), 949–
149 955. <https://doi.org/10.1038/s41561-021-00850-w>
- 150

Supplementary material for

Nonlinearity of the post-spinel transition and its expression in slabs and plumes worldwide

Junjie Dong^{1,2,*}, Rebecca A. Fischer¹, Lars Stixrude³, Matthew C. Brennan¹, Kierstin Daviau^{1,a,b}, Terry-Ann Suer^{1,c}, Katlyn M. Turner^{1,d}, Yue Meng⁴, Vitali B. Prakapenka⁵.

¹ Department of Earth and Planetary Sciences, Harvard University, Cambridge, Massachusetts, United States of America.

² Department of the History of Science, Harvard University, Cambridge, Massachusetts, United States of America.

³ Department of Earth, Planetary, and Space Sciences, University of California, Los Angeles, California, United States of America.

⁴ High Pressure Collaborative Access Team (HPCAT), X-Ray Science Division, Argonne National Laboratory, Argonne, Illinois, United States of America.

⁵ Center for Advanced Radiation Sources, University of Chicago, Chicago, Illinois, United States of America.

^a Now at Toi-Ohomai Institute of Technology, Tauranga, New Zealand.

^b Now at School of Science, University of Waikato, Tauranga, New Zealand.

^c Now at Laboratory for Laser Energetics, University of Rochester, Rochester, New York, United States of America.

^d Now at MIT Media Lab, Massachusetts Institute of Technology, Cambridge, Massachusetts, United States of America.

* Corresponding author: Junjie Dong (junjiedong@g.harvard.edu)

Contents of this file

Text S1 to S6

Figures S1 to S5

Tables S1 to S6

Supplementary Text:

S1: Additional details of experimental procedures

Short symmetric cells and a gas-membrane cell were used with 300 μm culet diamonds anvils to generate high pressure. Re gaskets were pre-indented to 20–28 GPa using the ruby fluorescence pressure and diamond anvil Raman (Akahama & Kawamura, 2006; Dewaele et al., 2008), and the Re gaskets were drilled to form a sample chamber with 120 μm diameter.

Starting material was powdered synthetic forsterite Mg_2SiO_4 (Alfa Aesar, synthetic, 99%). W powder (Alfa Aesar, puratronic, 99.999%) was ground and mixed in with the sample material in a ratio of ~1:3 by volume using a ball mill. The bulk composition and homogeneity of the starting material were confirmed by energy-dispersive X-ray spectroscopy (EDS). The powder mixtures were compressed between two diamond anvils to form a flake ~10 μm thick, then loaded between two layers of KCl. The KCl powder was oven-dried for at least 6 hours before sample loading. The samples were handled under clean, dry conditions at all stages of preparation and baked at 393–413 K (120–140 °C) under vacuum for 1–7 hours to remove residual moisture after loading but before closing the cell.

During laser heating, the sample was heated from both sides by two identical Yb fiber lasers ($\lambda = 1064 \text{ nm}$). The X-ray beam was monochromatized to a wavelength of 0.3344 Å and focused to an area of 5.3 $\mu\text{m} \times 4.4 \mu\text{m}$ at GESCARS, and to a wavelength of 0.4066 Å and focused to an area of 2.9 $\mu\text{m} \times 4.8 \mu\text{m}$ at HPCAT. Diffraction images were recorded with X-ray exposure times of 3–60 seconds and then were integrated into 1-D patterns using Dioptas (Prescher & Prakapenka, 2015).

Backgrounds of the integrated XRD patterns were identified using the least-squares fit of the Chebyshev series to data (implemented with the *NumPy* package in Python, Harris et al., 2020) and then subtracted. The peaks of W and KCl were identified and fitted with a combination of Gaussians, Lorentzians, and Voigt functions (implemented with the *lmfit* package in Python, Newville et al., 2014; Ostrouchov, 2018), and their 2θ values (related to the angles of diffraction) were estimated and used to calculate the unit cell parameters of W and KCl. Typically, the diffraction lines of (110), (200), (211), (220), (310) and (321) were used to determine the unit cell volume of W; (110), (200), (211) and (220) for the unit cell volume of KCl. The diffraction lines, their precision, and the propagated error to pressure were reported with the estimated pressure for each data point in Table S1.

S2: Additional details of phase identification and phase boundary detection

In general, 1) we used the first appearance of the peaks from the newly formed phase(s) between two consecutive diffraction patterns to detect phase transition, and 2) we tracked the trend of the peak intensity of the existing phase(s) between the phase boundaries detected in each heating cycle. The downside of the second criterion is that changes in peak intensity may also result from the non-random orientation of a small number of newly formed crystal grains and/or peak sharpening upon heating (e.g., Chanyshv et al., 2022). Therefore, as an additional criterion, we relied on the “spottiness” of Debye rings in the 2D XRD images to track the stability of existing phase(s) when the intensity of their diffraction peaks does not change in the same direction. In addition, to avoid mistaking variations in peak intensity and location caused by temperature drop for phase transitions, we excluded any diffraction pattern with a temperature drop of >50 K in the heating path.

One of the goals of this study is to explore the location of the Mg_2SiO_4 triple point as well as the high-temperature area between the triple point and the solidus. To reach this target P – T range (~ 21 – 23 GPa and 1900 – 2300 K), we started some of our experiments 3 – 4 GPa lower than this target pressures to account for the thermal pressure upon heating (from ~ 17 – 20 GPa and 1300 – 1600 K). This choice means that the newly formed rw and the relic wd often coexist throughout most of the experiment because the P – T conditions are close to the $wd \leftrightarrow rw$ phase boundary (with a lower reaction rate when approaching the boundary, Chanyshv et al., 2022). Wd with the orthorhombic structure has a much higher density of diffraction peaks than rw with the cubic structure, most of which are located near corresponding cubic features in the XRD patterns, which makes the detection of the first appearance of rw peaks particularly challenging.

Ideally, we would want to reverse the P – T path and observe the phase transitions again upon cooling. In practice, however, it is difficult to completely recombine the dissociated $bm + pe$ back to one single phase upon cooling for the time frame allowed for fast-paced synchrotron experiments due to a slow diffusion rate (Shimojuku et al., 2014) and the separation of the bm and pe grains (Ishii et al., 2018). Reversed experiments are often only feasible in multi-anvil experiments because the compression-decompression cycle and heating-cooling cycle can be controlled simultaneously and in small increments by a resistance heater and a hydraulic ram. However, the accuracy of temperature measurements in a multi-anvil press is limited by the thermocouple calibrations, and the pressure effects on emf remains unconstrained experimentally at $>\sim 1000$ K and, for example, would introduce a systematic temperature error of >80 K at 1773 K for the type D thermocouple, which significantly affects the determination of Clapeyron slopes (Nishihara et al., 2020). Therefore, LH-DAC experiments provide an effective way to collect a relatively large dataset with less systematic errors (at the cost of larger random errors) in temperature measurements.

S3: Additional details of the selection of phase stability observations from literature.

Historically, experimental studies determined the P - T conditions of a phase transition using the ex situ method, and these ex situ studies (e.g., Ito & Takahashi, 1989; Ishii et al., 2011) reported pressures based on “fixed point” calibrations (typically with one at room temperature and one at high temperature, e.g., Irifune et al., 2014). In these ex situ experiments, however, pressure usually varies with temperature, and this temperature dependence of pressure is a complex function of thermal pressure and material relaxation and depends on the P - T path of the run (Fei et al., 2004). It is difficult to compare and correct the pressures of these ex situ datasets, and we hence excluded them from the compilation. For temperature correction, one in situ study, Fei et al. (2004), used the type C ($W_{95}Re_5$ - $W_{74}Re_{26}$) thermocouple; No extrapolatable calibration of its pressure effects is available for the type C thermocouple (Li et al., 2003). Therefore, we also excluded the Fei et al., (2004) dataset from the compilation. These excluded datasets represent only a very small fraction of total data points of our data compilation, and they had minimal effects on the location and slope of the post-spinel boundary when they were included in the global analysis.

S4: Additional details of machine learning procedures

In the framework of supervised learning (Fig. S2), the data compilation was first split into a train set (70%) and a test set (30%). The multi-class logistic model for the Mg_2SiO_4 phase boundaries would be eventually evaluated on both the train set and test set because the model could overfit the train set to predict perfect responses but fail to perform well in the unseen test set. In this study, we used the polynomials of P and T by degree 1 to 5 to describe a phase boundary. Overfitting might occur without supervised learning if the degree of the polynomial we chose is too large, and to prevent overfitting, we applied a regularization method called *Lasso*, or L_1 regularization. The regularization method *constrains* or *regularizes* the coefficient estimates, β_j , by modifying the least-squares loss function, $\mathcal{L}(\beta)$, into a regularized loss function, $\mathcal{L}_{\text{Lasso}}(\beta) = \mathcal{L}(\beta) + \lambda \sum_{i,j=1}^n |\beta_{i,j}|$, where λ is a scaler that assigns weights to the regularization term, or the regularization strength, $\lambda \sum_{i,j=1}^n |\beta_{i,j}|$. We then used λ to discourage/penalize extreme values of β_j to avoid overfitting: when λ is sufficiently large, the regularized loss function $\mathcal{L}_{\text{Lasso}}(\beta)$ becomes increasingly sensitive to $\lambda \sum_{i,j=1}^n |\beta_{i,j}|$; in such scenario, a successful convergence would shrink β_{Lasso} to zero, or close to zero.

The hyperparameter (C), or the inverse of regularization strength ($\lambda = \frac{1}{C}$), along with other parameter choices in the *scikit-learn* package including “multi_class” (classification strategies) and “solver” (algorithms to use in the optimization problem), need to be tuned to optimize the multi-class logistic models. We performed (hyper-)parameter tuning using grid search with k -fold cross-validation, in which the train set was further split into k folds ($k = 3-5$): the model was trained using $k-1$ of the small folds, and the resulting model was validated on the reminder of the train set, a single fold held out as the validation set. The final evaluation of the parameters was based on the average over the k folds.

The next step was to choose an evaluation metric. Two common metrics are *precision* ($\frac{\text{true positive}}{\text{true positive} + \text{false positive}}$) and *recall* ($\frac{\text{true positive}}{\text{true positive} + \text{false negative}}$): for example, if we were to draw a phase boundary between rw and $bm + pe$, precision describes the proportion of the data points the estimated phase boundary identified as rw actually were rw ; while recall describes the proportion of all rw data points the estimated phase boundary actually identified as rw . The precision and recall of a model are inversely correlated, and in phase diagram determination, we need to maximize both precision and recall. So, their harmonic mean is used as the evaluation metric, F_1 score ($2 \times \frac{\text{precision} \times \text{recall}}{\text{precision} + \text{recall}}$) and it has the advantage of penalizing extreme values. A high F_1 score means a better balance between precision and recall. The hyperparameter-tuned model was then fit to the train set and test set, and the degree of polynomial that has the maximum F_1 score on the test set became the best-fit model. Then, we used the multi-class logistic regression with the selected degree of polynomial to fit the original data set (the train and test set recombined) and produced a statistically-optimized phase diagram.

S5: A brief review of previous data and their comparison with this study.

To benchmark the logistic model used in this study, we applied the simple binary logistic model (Kavner et al., 2011) with the assumption of a linear boundary to the individual uncorrected literature dataset. The phase boundaries redetermined by on the logistic models in general agree with the free-hand drawn boundaries, which validates the logistic functions as a model to describe phase stability observations. We now review previous individual experimental datasets and compare it with our global analysis:

- 1) The Clapeyron slope of the post-spinel transition in Mg_2SiO_4 has been studied extensively because of its relevance to the “660-km” seismic discontinuity, and except for Chanyshv et al. (2022), the majority of the literature assumed a linear boundary. Earlier experimental studies usually report a more negative Clapeyron slope for the post-spinel boundary, -3 – -4 MPa/K (Ito & Yamada, 1982; Ito & Takahashi, 1989; Ito et al., 1990; Akaogi & Ito, 1993; Chopelas et al., 1994; Irifune et al., 1998); the pressures reported by these earlier studies were determined ex situ based on “fixed-point” calibrations, so they were more susceptible to systematic biases than in situ pressure scales (Li, 2022). More recent work with improved experimental techniques (e.g., pressure determination, phase identification, etc.) suggest the post-spinel slope is less negative, from -1 – -2 to virtually 0 MPa/K (Katsura et al., 2003; Fei et al., 2004; Ghosh et al., 2013; Ishii et al., 2011; Ghosh et al., 2013; Chanyshv et al., 2022). The estimates on the post-spinel Clapeyron slope have become less negative over several decades of experimental investigation. This trend suggests inadequate assumption of the linear boundary that would cause overestimation of the post-spinel Clapeyron slope magnitude if it was averaged over a larger temperature range: indeed, earlier experimental studies that reported the slopes of -3 – -4 MPa/K typically averaged their slopes between 1200 to 2100 K while more recent works averaged their slopes of -1 – -2 MPa/K over 1600 to 2100 K. The nonlinearity we introduced in this study rendered the multi-class logistic model to capture the increasing negative post-spinel slope that the linear assumption was insufficient to describe.
- 2) We also found a nearly vertical $wd \leftrightarrow bm + pe$ boundary of $0.4_{-2.9}^{+1.8}$ MPa/K at 2400 ± 200 K, which is generally consistent with the dataset reported by Chudinovskikh & Boehler (2001) and Hirose (2002). The Chudinovskikh & Boehler (2001) dataset is uncorrectable due to the lack of the EoS information about its pressure scales, so it is not included in our compilation and therefore can be considered as an independent test. Hirose (2002) suggested a slightly negative $wd \leftrightarrow bm + pe$ slope (~ -2 MPa/K), but its slope was only implied by a single pair of experimental brackets at 2273 K, so its slope was not effectively constrained. In general, the $wd \leftrightarrow bm + pe$ slope remains less well constrained even with the compiled dataset, due to the increasingly scattered data above the triple point.
- 3) Lastly, we found a $wd \leftrightarrow rw$ slope of $6.2_{-1.1}^{+1.6}$ MPa/K at 1800 ± 200 K, which is consistent with the free-hand drawn slopes reported by Katsura & Ito (1989) and Suzuki et al. (2000) (~ 7 MPa/K) and slightly more positive than the free-hand drawn slopes from Kuroda et al. (2000) and Inoue et al. (2006) (~ 3 – 4 MPa/K). A relatively more positive slope between 1500 and 2100 K is more consistent with the corrected experimental observations and it is also more consistent with the

phase diagram globally because a relatively linear $w d \leftrightarrow r w$ slope of $\sim 3\text{--}4$ MPa/K would intersect and form at a triple point that does not agree with the majority of the $w d \leftrightarrow b m + p e$ boundary observations (Chudinovskikh & Boehler, 2001; Hirose, 2002; this study). We noticed that the redetermined $w d \leftrightarrow r w$ slope (~ 1 MPa/K) from the Suzuki et al. (2000) data is significantly smaller than the values originally reported (~ 7 MPa/K); it implies that the $w d \leftrightarrow r w$ boundary may become much more nonlinear when temperature is lower than 1500 K. Unfortunately, the low-temperature constraints on the $w d \leftrightarrow r w$ boundary are still lacking; our speculation on the nonlinearity of the $w d \leftrightarrow r w$ boundary below 1500 K requires future experimental evidence to confirm.

S6: Additional details of the composite mantle temperature model for the “660-km” discontinuity.

The composite mantle temperature model for the “660-km” discontinuity estimates the lateral variations in the mantle temperature at the “660-km” depths, T_{660} (Fig. 5a). It combines three existing thermal models derived from seismic, geophysical and geodynamical constraints: 1) 2D kinematic models for subducting slabs (Syracuse et al., 2010), 2) global shear velocity constraints for plume-fed hotspots (Bao et al., 2022), and 3) globally compiled S660S observations for the ambient mantle (Waszek et al., 2021).

To extrapolate slab temperatures to the “660-km” depth, we used the P – T paths of the slab surface for all arc segments from the W1300 case of Syracuse et al. (2010) (up to 250 km). The gradients of most subduction temperature profiles become virtually constant after 150 km (~ 5 GPa) and vary between 0.3 and 0.5 K/km (Shirey et al., 2021). We, therefore, calculated the average slope of each subduction temperature profile between 150–250 km (~ 5 –8 GPa) and then estimated the T_{660} for each subduction segment by extrapolating their P – T paths to the 660-km depth with their respective temperature gradient.

Our estimates of the T_{660} for plume-fed oceanic hotspots were obtained based on their mantle potential temperature estimates reported by Bao et al. (2022) (Table S6). We first calculated the mantle adiabats for each plume-fed oceanic hotspot with their respective mantle potential temperature using HeFESTo, assuming a depleted MORB mantle (DMM). We then took the mantle temperature at the “660-km” depth along the respective mantle adiabat as the T_{660} for that specific hotspot.

Similarly, our estimates of the T_{660} for the ambient mantle were extrapolated from the global mantle potential temperature map reported by Waszek et al. (2021). We calculated the mantle adiabats for each geographical location based on their respective mantle potential temperature using HeFESTo, assuming a mechanically mixed (MM) mantle of 20% basalt and 80% harzburgite. We then took the mantle temperature at the “660-km” depth along the respective mantle adiabat as the T_{660} for that specific geographical location.

The simple extrapolations we used here to estimate T_{660} may introduce significant errors. For example, slab geometry may vary significantly beyond 250 km for some arc segments, and our assumption of the constant temperature gradient for all slab segments is likely unrealistic. The actual mantle temperatures for some slab segments at the “660-km” depths may deviate from our estimates. With that being said, this composite T_{660} model serves as reasonable first-order approximations for the lateral variation of mantle temperature across the “660-km” discontinuity.

Supplementary Figures:

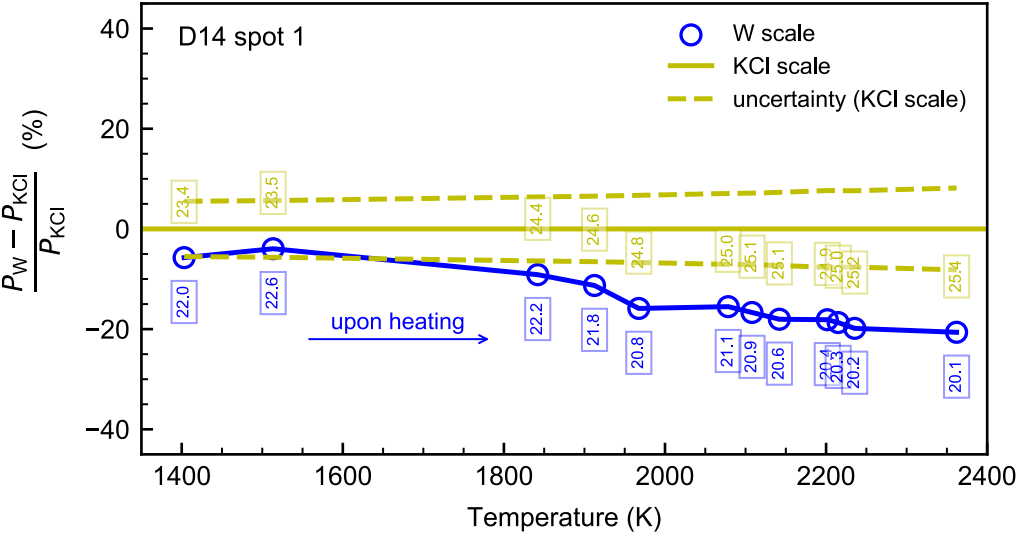


Figure S1: Difference between pressures (in GPa) calculated based on the W scale (Sokolova et al., 2016) and pressures based on the KCl scale (Tateno et al., 2019). The P_W estimates deviate significantly from those of P_{KCl} at high temperatures, likely due to lack of thermal EoS data on W at $>\sim 1673$ K (Litasov et al., 2013; Sokolova et al., 2016). Therefore, we chose KCl as our primary pressure scale, and all pressures reported in the main text are based on the EoS of KCl from Tateno et al., (2019) The P_W estimates upon heating in D14 spot 1 are plotted in blue circles; their respective P_{KCl} estimates are plotted in a solid yellow line with the uncertainty range in dashed yellow lines.

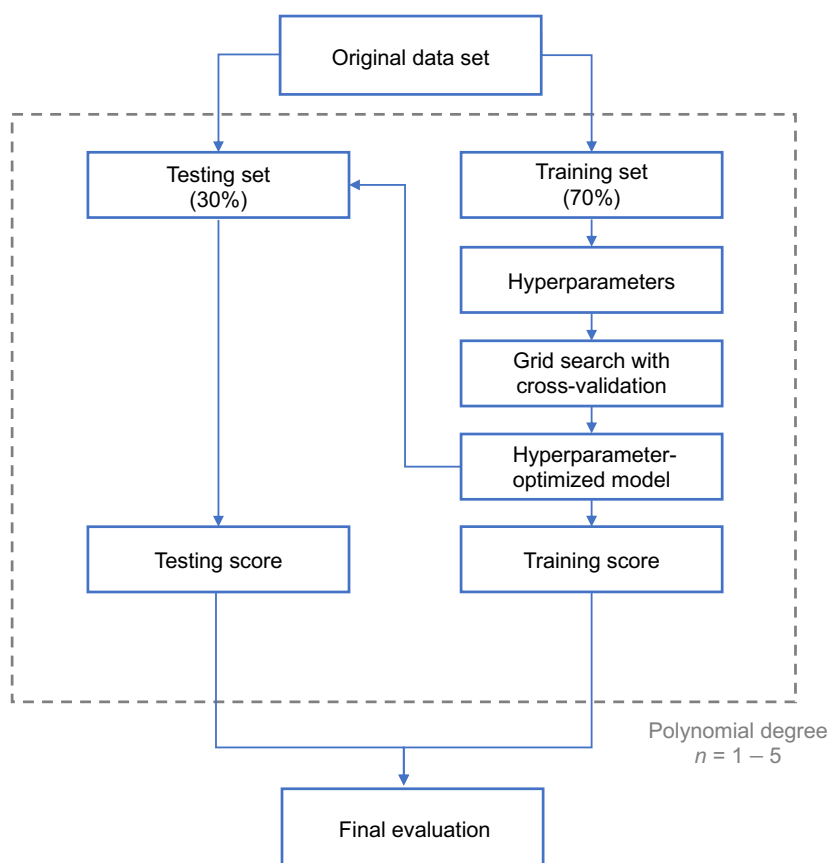


Figure S2: Flow chart of machine learning procedure. The original dataset is split into two sets: a training set (70%) and a testing set (30%). With the training dataset, hyperparameters in the multi-class logistic model are optimized using grid searching with cross-validation. The F_1 scores are estimated for the hyperparameter-optimized multi-class logistic models of the polynomials by degree 1 to 5 on the train set and test set, respectively; The best model is selected based on the F_1 score of the testing set in the final evaluation.

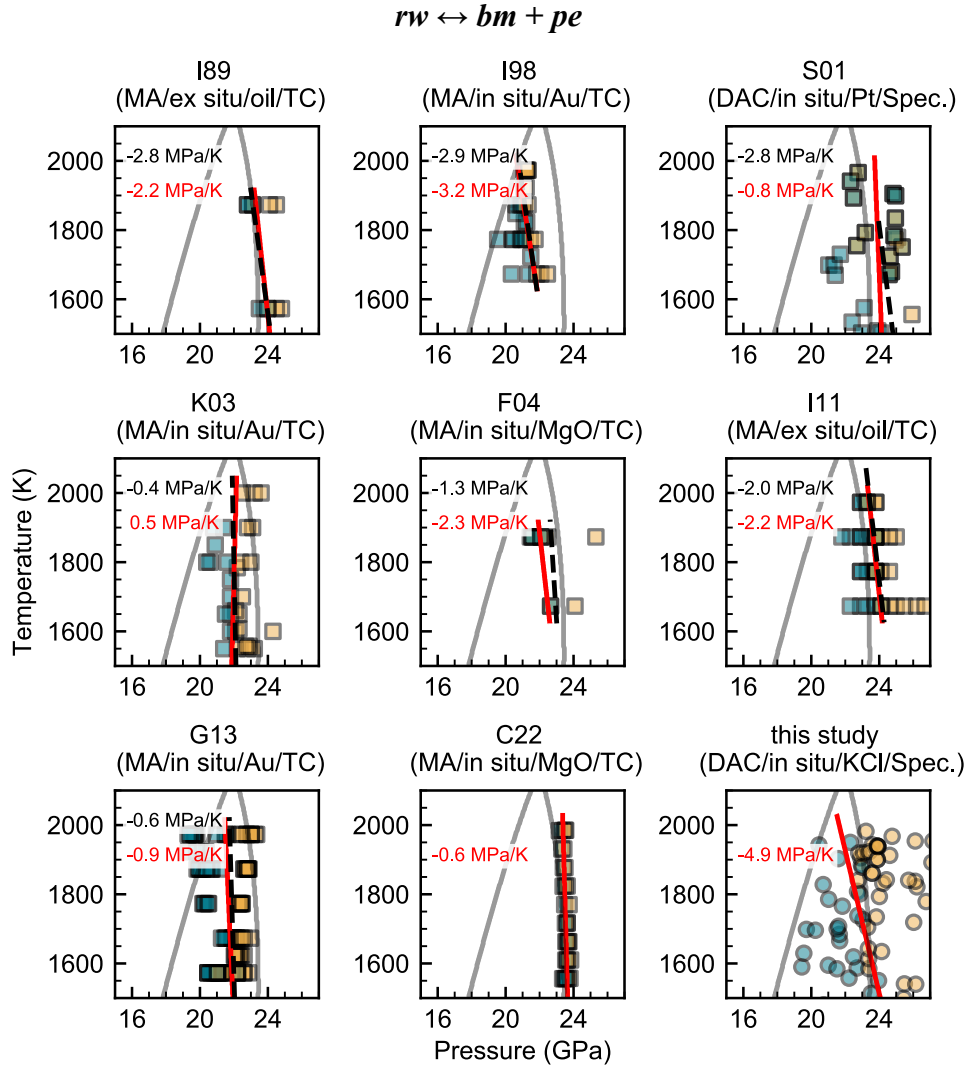


Figure S3: Benchmarks on the $rw \leftrightarrow bm + pe$ post-spinel transition with the simple binary logistic model for each literature dataset. Phase stability observations on rw and $bm + pe$ are color-coded in blue and yellow, respectively. Phase boundaries predicted by the simple binary logistic models are plotted as solid red lines while the free-hand drawn phase boundaries previously reported by their respective studies are plotted as dashed black lines. Clapeyron slopes estimated by the simple binary logistic models and free-hand drawing are shown in red and black, respectively. Additional information about the literature dataset is listed above each subplot, including the abbreviations for the relevant study, the type of high pressure techniques used, whether the data was collected in situ or ex situ, the type of pressure scale or calibration used, and the type of temperature measurement. The following abbreviations are used: I89, Ito & Takahashi (1989); I98, Irifune et al. (1998); S01, Shim et al. (2001); K03, Katsura et al. (2003); F04, Fei et al. (2004); I11, Ishii et al. (2011); G13, Ghosh et al. (2013); C22, Chanyshev et al. (2022); MA, multi-anvil press; DAC, diamond anvil cell; TC, thermocouple; Spec., spectroradiometer.

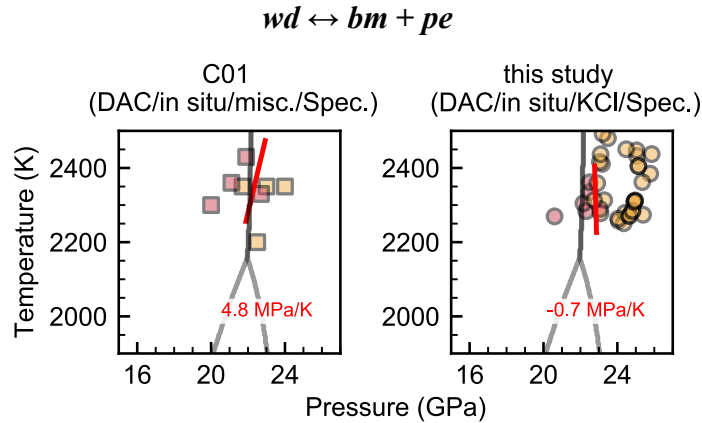


Figure S4: Benchmarks on the $wd \leftrightarrow bm + pe$ transition with the simple binary logistic model for each literature dataset. Phase stability observations on wd and $bm + pe$ are color-coded in red and yellow, respectively. Phase boundaries predicted by the simple binary logistic models are plotted as solid red lines. Clapeyron slopes estimated by the simple binary logistic models are shown in red. Additional information about the literature dataset is listed above each subplot, including the abbreviations for the relevant study, the type of high pressure techniques used, whether the data was collected in situ or ex situ, the type of pressure scale or calibration used, and the type of temperature measurement. The following abbreviations are used: C01, Chudinovskikh & Bohler (2001); DAC, diamond anvil cell; Spec., spectroradiometer; misc., miscellaneous pressure scales.

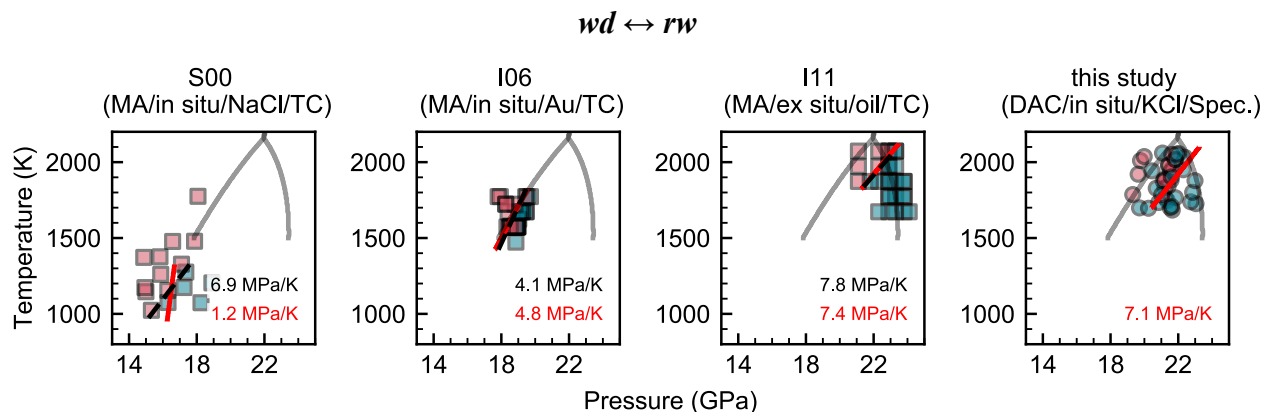


Figure S5: Benchmarks on the $wd \leftrightarrow rw$ transition with the simple binary logistic model for each literature dataset. Phase stability observations on wd and rw are color-coded in red and blue, respectively. Phase boundaries predicted by the simple binary logistic models are plotted as solid red lines while the free-hand drawn phase boundaries previously reported by their respective studies are plotted as dashed black lines. Clapeyron slopes estimated by the simple binary logistic models and free-hand drawing are shown in red and black, respectively. Additional information about the literature dataset is listed above each subplot, including the abbreviations for the relevant study, the type of high pressure techniques used, whether the data was collected in situ or ex situ, the type of pressure scale or calibration used, and the type of temperature measurement. The following abbreviations are used: S00, Suzuki et al. (2000); I06, (Inoue et al., 2006); I11, Ishii et al. (2011); MA, multi-anvil press; DAC, diamond anvil cell; TC, thermocouple; Spec., spectroradiometer.

Supplementary Tables:

(For Tables S1–S6, please see the Excel spreadsheets attached.)

Table S1: New in situ experimental dataset on the Mg_2SiO_4 phase diagram.

Table S2: In situ phase stability observations in Mg_2SiO_4 compiled from literature with corrected pressures and temperatures.

Table S3: In situ and ex situ phase stability observations in Mg_2SiO_4 compiled from literature with uncorrected pressures and temperatures.

Table S4: Model selection results.

Table S5: Subducting slabs and their T_{660} and $\gamma_{\text{postspinel}}$.

Table S6: Hotspot-associated plumes and their T_{660} and $\gamma_{\text{postspinel}}$.

References:

- Akahama, Y., & Kawamura, H. (2006). Pressure calibration of diamond anvil Raman gauge to 310 GPa. *Journal of Applied Physics*, *100*(4). <https://doi.org/10.1063/1.2335683>
- Akaogi, M., & Ito, E. (1993). Refinement of enthalpy measurement of MgSiO₃ perovskite and negative pressure-temperature slopes for Perovskite-forming reactions. *20*(17), 1839–1842.
- Bao, X., Lithgow-Bertelloni, C. R., Jackson, M. G., & Romanowicz, B. (2022). On the relative temperatures of Earth's volcanic hotspots and mid-ocean ridges. *Science*, *375*, 57–61. <https://doi.org/http://dx.doi.org/10.1126/science.abj8944>
- Chanyshev, A., Ishii, T., Bondar, D., Bhat, S., Kim, E. J., Farla, R., Nishida, K., Liu, Z., Wang, L., Nakajima, A., Yan, B., Tang, H., Chen, Z., Higo, Y., Tange, Y., & Katsura, T. (2022). Depressed 660-km discontinuity caused by akimotoite–bridgmanite transition. *Nature*, *601*(7891), 69–73. <https://doi.org/10.1038/s41586-021-04157-z>
- Chopelas, A., Boehler, R., & Ko, T. (1994). Thermodynamics and Behavior of γ -Mg₂SiO₄ at High Pressure: Implications for Mg₂SiO₄ Phase Equilibrium. In *Phys Chem Minerals* (Vol. 21).
- Chudinovskikh, L., & Boehler, R. (2001). High-pressure polymorphs of olivine and the 660-km seismic discontinuity. *Nature*, *411*, 574–577. <https://doi.org/10.1038/35079060>
- Dewaele, A., Torrent, M., Loubeyre, P., & Mezouar, M. (2008). Compression curves of transition metals in the Mbar range: Experiments and projector augmented-wave calculations. *Physical Review B - Condensed Matter and Materials Physics*, *78*(10). <https://doi.org/10.1103/PhysRevB.78.104102>
- Fei, Y., van Orman, J., Li, J., van Westrenen, W., Sanloup, C., Minarik, W., Hirose, K., Komabayashi, T., Walter, M., & Funakoshi, K. (2004). Experimentally determined postspinel transformation boundary in Mg₂SiO₄ using MgO as an internal pressure standard and its geophysical implications. *Journal of Geophysical Research: Solid Earth*, *109*(B2). <https://doi.org/10.1029/2003jb002562>
- Ghosh, S., Ohtani, E., Litasov, K. D., Suzuki, A., Dobson, D., & Funakoshi, K. (2013). Effect of water in depleted mantle on post-spinel transition and implication for 660km seismic discontinuity. *Earth and Planetary Science Letters*, *371–372*, 103–111. <https://doi.org/10.1016/j.epsl.2013.04.011>
- Harris, C. R., Millman, K. J., van der Walt, S. J., Gommers, R., Virtanen, P., Cournapeau, D., Wieser, E., Taylor, J., Berg, S., Smith, N. J., Kern, R., Picus, M., Hoyer, S., van Kerkwijk, M. H., Brett, M., Haldane, A., del Río, J. F., Wiebe, M., Peterson, P., ... Oliphant, T. E. (2020). Array programming with NumPy. *Nature*, *585*(7825), 357–362. <https://doi.org/10.1038/s41586-020-2649-2>
- Hirose, K. (2002). Phase transitions in pyrolitic mantle around 670-km depth: Implications for upwelling of plumes from the lower mantle. *Journal of Geophysical Research: Solid Earth*, *107*(B4), ECV 3-1-ECV 3-13. <https://doi.org/10.1029/2001jb000597>
- Inoue, T., Irifune, T., Higo, Y., Sanehira, T., Sueda, Y., Yamada, A., Shinmei, T., Yamazaki, D., Ando, J., Funakoshi, K., & Utsumi, W. (2006). The phase boundary between wadsleyite and ringwoodite in Mg₂SiO₄ determined by in situ X-ray diffraction. *Physics and Chemistry of Minerals*, *33*(2), 106–114. <https://doi.org/10.1007/s00269-005-0053-y>
- Irifune, T., Isobe, F., & Shinmei, T. (2014). A novel large-volume Kawai-type apparatus and its application to the synthesis of sintered bodies of nano-polycrystalline diamond. *Physics of the Earth and Planetary Interiors*, *228*, 255–261. <https://doi.org/10.1016/j.pepi.2013.09.007>
- Irifune, T., Nishiyama, N., Kuroda, K., Inoue, T., Isshiki, M., Utsumi, W., Urakawa, S., Uchida, T., & Ohtaka, O. (1998). The Postspinel Phase Boundary in Mg₂SiO₄ Determined by in Situ X-ray Diffraction. *Science*, *279*(5357), 1698–1700. <https://doi.org/10.1126/science.279.5357.1698>

- Ishii, T., Huang, R., Fei, H., Koemets, I., Liu, Z., Maeda, F., Yuan, L., Wang, L., Druzhbin, D., Yamamoto, T., Bhat, S., Farla, R., Kawazoe, T., Tsujino, N., Kulik, E., Higo, Y., Tange, Y., & Katsura, T. (2018). Complete agreement of the post-spinel transition with the 660-km seismic discontinuity. *Scientific Reports*, 8(1). <https://doi.org/10.1038/s41598-018-24832-y>
- Ishii, T., Kojitani, H., & Akaogi, M. (2011). Post-spinel transitions in pyrolite and Mg₂SiO₄ and akimotoite-perovskite transition in MgSiO₃: Precise comparison by high-pressure high-temperature experiments with multi-sample cell technique. *Earth and Planetary Science Letters*, 309(3–4), 185–197. <https://doi.org/10.1016/j.epsl.2011.06.023>
- Ito, E., Akaogi, M., Topor, L., & Navrotsky, A. (1990). Negative Pressure-Temperature Slopes for Reactions Forcing MgSiO₃ Perovskite from Calorimetry. *Science*, 249(4974), 1275–1278. <https://doi.org/10.1126/science.249.4974.1275>
- Ito, E., & Takahashi, E. (1989). Postspinel transformations in the system Mg₂SiO₄-Fe₂SiO₄ and some geophysical implications. *Journal of Geophysical Research*, 94(B8). <https://doi.org/10.1029/jb094ib08p10637>
- Ito, E., & Yamada, H. (1982). Stability relations of silicate spinels, ilmenite and perovskites. In S. Akimoto & M. Manghnani (Eds.), *High Pressure Research in Geophysics* (pp. 405–419). D. Reidel.
- Katsura, T., & Ito, E. (1989). The system Mg₂SiO₄-Fe₂SiO₄ at high pressures and temperatures: precise determination of stabilities of olivine, modified spinel, and spinel. *Journal of Geophysical Research*, 94(B11). <https://doi.org/10.1029/jb094ib11p15663>
- Katsura, T., Yamada, H., Shinmei, T., Kubo, A., Ono, S., Kanzaki, M., Yoneda, A., Walter, M. J., Ito, E., Urakawa, S., Funakoshi, K., & Utsumi, W. (2003). Post-spinel transition in Mg₂SiO₄ determined by high P - T in situ X-ray diffractometry. *Physics of the Earth and Planetary Interiors*, 136(1–2), 11–24. [https://doi.org/10.1016/S0031-9201\(03\)00019-0](https://doi.org/10.1016/S0031-9201(03)00019-0)
- Kavner, A., Speed, T., & Jeanloz, R. (2011). Statistical Analysis of Phase-Boundary Observations. In *Physics Meets Mineralogy* (pp. 71–80). Cambridge University Press. <https://doi.org/10.1017/cbo9780511896590.006>
- Kuroda, K., Irifune, T., Inoue, T., Nishiyama, N., Miyashita, M., Funakoshi, K., & Utsumi, W. (2000). Determination of the phase boundary between ilmenite and perovskite in MgSiO₃ by in situ X-ray diffraction and quench experiments. *Physics and Chemistry of Minerals Volume*, 27, 523–532. <https://doi.org/https://doi.org/10.1007/s002690000096>
- Li, J. (2022). Synthesis of high-pressure silicate polymorphs using multi-anvil press. In Y. Fei & M. J. Walter (Eds.), *Static and Dynamic High Pressure Mineral Physics*. Cambridge University Press.
- Li, J., Hadidiacos, C., Mao, H. K., Fei, Y., & Hemley, R. J. (2003). Behavior of thermocouples under high pressure in a multi-anvil apparatus. *High Pressure Research*, 23(4), 389–401. <https://doi.org/10.1080/0895795031000088269>
- Litasov, K. D., Gavryushkin, P. N., Dorogokupets, P. I., Sharygin, I. S., Shatskiy, A., Fei, Y., Rashchenko, S. v., Seryotkin, Y. v., Higo, Y., Funakoshi, K., & Ohtani, E. (2013). Thermal equation of state to 33.5 GPa and 1673 K and thermodynamic properties of tungsten. *Journal of Applied Physics*, 113(13). <https://doi.org/10.1063/1.4799018>
- Newville, M., Stensitzki, T., Allen, D. B., & Ingargiola, A. (2014). *LMFIT: Non-Linear Least-Square Minimization and Curve-Fitting for Python*. Zenodo. <https://doi.org/10.5281/zenodo.11813>
- Nishihara, Y., Doi, S., Kakizawa, S., Higo, Y., & Tange, Y. (2020). Effect of pressure on temperature measurements using WRe thermocouple and its geophysical impact. *Physics of the Earth and Planetary Interiors*, 298. <https://doi.org/10.1016/j.pepi.2019.106348>

- Ostrouchov, C. (2018, April 13). *Peak fitting XRD data with Python*.
https://chrisostrouchov.com/post/peak_fit_xrd_python/
- Prescher, C., & Prakapenka, V. B. (2015). DIOPTAS: A program for reduction of two-dimensional X-ray diffraction data and data exploration. *High Pressure Research*, 35(3), 223–230.
<https://doi.org/10.1080/08957959.2015.1059835>
- Shim, S.-H., Duffy, T. S., & Shen, G. (2001). The post-spinel transformation in Mg₂SiO₄ and its relation to the 660-km seismic discontinuity. *Nature*, 411, 571–574.
<https://doi.org/10.1038/35079053>
- Shimajuku, A., Boujibar, A., Yamazaki, D., Yoshino, T., Tomioka, N., & Xu, J. (2014). Growth of ringwoodite reaction rims from MgSiO₃ perovskite and periclase at 22.5 GPa and 1,800 °C. *Physics and Chemistry of Minerals*, 41(7), 555–567. <https://doi.org/10.1007/s00269-014-0669-x>
- Shirey, S. B., Wagner, L. S., Walter, M. J., Pearson, D. G., & van Keken, P. E. (2021). Slab Transport of Fluids to Deep Focus Earthquake Depths—Thermal Modeling Constraints and Evidence From Diamonds. *AGU Advances*, 2(2). <https://doi.org/10.1029/2020av000304>
- Sokolova, T. S., Dorogokupets, P. I., Dymshits, A. M., Danilov, B. S., & Litasov, K. D. (2016). Microsoft excel spreadsheets for calculation of P–V–T relations and thermodynamic properties from equations of state of MgO, diamond and nine metals as pressure markers in high-pressure and high-temperature experiments. *Computers and Geosciences*, 94, 162–169.
<https://doi.org/10.1016/j.cageo.2016.06.002>
- Suzuki, A., Ohtani, E., Morishima, H., Kubo, T., Kanbe, Y., Kondo, T., Okada, T., Terasaki, H., Kato, T., & Kikegawa, T. (2000). In situ determination of the phase boundary between wadsleyite and ringwoodite in Mg₂SiO₄. *Geophysical Research Letters*, 27(6), 803–806.
<https://doi.org/10.1029/1999GL008425>
- Syracuse, E. M., van Keken, P. E., Abers, G. A., Suetsugu, D., Bina, C., Inoue, T., Wiens, D., & Jellinek, M. (2010). The global range of subduction zone thermal models. *Physics of the Earth and Planetary Interiors*, 183(1–2), 73–90. <https://doi.org/10.1016/j.pepi.2010.02.004>
- Tateno, S., Komabayashi, T., Hirose, K., Hirao, N., & Ohishi, Y. (2019). Static compression of B2 KCl to 230 GPa and its P-V-T equation of state. *American Mineralogist*, 104(5), 718–723.
<https://doi.org/10.2138/am-2019-6779>
- Waszek, L., Tauzin, B., Schmerr, N. C., Ballmer, M. D., & Afonso, J. C. (2021). A poorly mixed mantle transition zone and its thermal state inferred from seismic waves. *Nature Geoscience*, 14(12), 949–955. <https://doi.org/10.1038/s41561-021-00850-w>